Space-charge dynamics in microdiodes

Marjan Ilkov

Doctor of Philosophy
November 2015
School of Science and Engineering
Reykjavík University

Ph.D. Dissertation

Space-charge dynamics in microdiodes

Dissertation of 30 ECTS credits submitted to the School of Science and Engineering
at Reykjavík University in partial fulfillment of
the requirements for the degree of
Doctor of Philosophy

November 2015

Thesis Committee:

Ágúst Valfells, Supervisor
Associate Professor, Reykjavík University, Iceland

Andrei Manolescu,
Professor, Reykjavík University, Iceland

Viðar Guðmundsson,
Professor, University of Iceland, Iceland

Allen Garner, Examiner
Associate Professor, Purdue University, USA

Space-charge dynamics in microdiodes

Marjan Ilkov

November 2015

Abstract

Space-charge limited emission in vacuum microdiodes can go through transverse modulation under certain conditions. The frequency of this modulated current is in the terahertz band and it can be tuned by changing either the the gap spacing or the gap voltage of the diode. Doing the latter is the preferred mode of operation during the simulations which we did. As the power of such diode radiators would be very small, we coupled arrays of such diodes and showed that such an array, which synchronizes itself, can give powerful enough radiation for practical usage. For the emission process, it was first assumed that electrons would be emitted with zero initial velocity, as such an assumption is readily used in most emission calculations in the room temperature range. To further the research, we assumed non-zero initial velocities for the photoemitted electrons and found that, although, not without effect, the non-zero initial velocity does not significantly reduce the power of the radiator. The spatial structure of the beams was examined as well. Finally, a code for simulation of the space-charge effects in solar cells was tested, and although at present no claims can be made about these effects, the code proved to be a very good tool which replicated results from experiments and theory alike. Further experimental research on the detection of space-charge limited currents and the associated Coulomb oscillations is needed.

Hreyfifræði rúm hleðsla í míkró díóðum

Marjan Ilkov

nóvember 2015

Útdráttur

Losun rafeinda frá díóðu í lofttæmi getur orðið fyrir láréttri mótun undir vissum skilyrðum. Tíðnin á þessum mótaða straumi getur verið á terahertz tíðni sviðinu og hægt er að stilla hana með því að breyta fjarlægð díóðu frá skauti og spennuni þar á milli. Seinni kosturinn er ákjósanlegri og sá möguleiki rannsakaður hér með tölvulíkani.
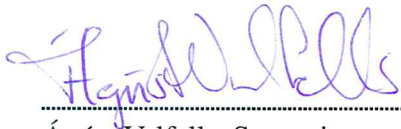
Aflið frá einni díóðu er frekar lítið og því eru mörgum díóðum raðað upp. Díóðunar samstilla sig og geta saman gefið frá sér nóg afl til að vera hagnýtanlegar. Í losunar ferli rafeindana var fyrst gert ráð fyrir að þær hefðu engan upphafshraða. Slík nálgun er oft gerð jafnavel við herbergishita. En til að ganga lengra gerðum við ráð fyrir að upphafshraða fyrir rafeindirnar og fundum að hann minnkar ekki mikið aflið. Dreifing rafeinda geislans var líka skoðuð. Í lokinn var tölvulíkani fyrir sólarrafhlöður notaður til að skoða áhrif hleðslanna á starfrækslu rafhlöðunnar. Kóðinn reyndist vera ágæt tæki og gat hermt eftir niðurstöðum úr tilraunum og svipuðum líkönum. Frekari rannsóknar er þörf á mettunar strauminn og Coulomb sveiflunum í slíkum kerfum.

x

The undersigned hereby certify that they recommend to the School of Science and Engineeringat Reykjavík University for acceptance this Dissertation entitled **Space-charge dynamics in microdiodes** submitted by **Marjan Ilkov** in partial fulfillment of the requirements for the degree of **Doctor of Philosophy (Ph.D.) in Applied Physics**
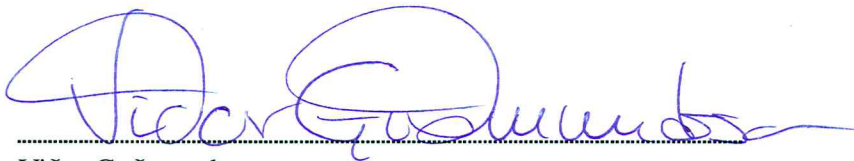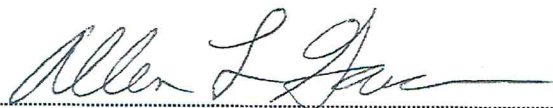
12.10.2015
....
date

....
Ágúst Valfells, Supervisor
Associate Professor, Reykjavík University, Iceland

....
Andrei Manolescu,
Professor, Reykjavík University, Iceland

....
Viðar Guðmundsson,
Professor, University of Iceland, Iceland

....
Allen Garner, Examiner
Associate Professor, Purdue University, USA

The undersigned hereby grants permission to the Reykjavík University Library to reproduce single copies of this Dissertation entitled **Space-charge dynamics in microdiodes** and to lend or sell such copies for private, scholarly or scientific research purposes only.

The author reserves all other publication and other rights in association with the copyright in the Dissertation, and except as herein before provided, neither the Dissertation nor any substantial portion thereof may be printed or otherwise reproduced in any material form whatsoever without the author's prior written permission.

12-10-2015
....
date

....
Marjan Ilkov
Doctor of Philosophy

I dedicate this work to my family.

Acknowledgements

Publications

This PhD thesis is based on the following publications:

A.) Palmar Jonsson, Marjan Ilkov, Andrei Manolescu, Andreas Pedersen, and Ágúst Valfells, "Tunability of the terahertz space-charge modulation in a vacuum microdiode", Phys. Plasmas, vol.21, 023107, 2013.

B.) Marjan Ilkov, Andreas Pedersen, Andrei Manolescu, Ágúst Valfells: Simulation of Self Organized Electron Beams in Vacuum Microdiodes. SIMULTECH 2013: 224-228

C.) Marjan Ilkov, Kristinn Torfason, Andrei Manolescu, Ágúst Valfells, "Synchronization in arrays of vacuum microdiodes", IEEE TRANSACTIONS ON ELECTRON DEVICES Volume: 62 Issue: 1 Pages: 200-206 Published: JAN 2015

D.) Marjan, Ilkov; Kristinn, Torfason; Andrei, Manolescu; Ágúst, Valfells, "Terahertz pulsed photogenerated current in microdiodes at room temperature", Appl. Phys. Lett. 107, 203508 (2015);

Abstracts, posters, oral presentations

- Ilkov, M.; Manolescu, A.; Valfells, Á ; Pedersen, A., "Vacuum microdiodes as tunable THZ oscillators," Plasma Science (ICOPS), 2013 Abstracts IEEE International Conference on , vol., no., pp.1,1, 16-21 June 2013 [1]

- Ilkov, M.; Torfason, K.; Manolescu, A.; Valfells, Á , "Synchronization of THz space-charge oscillation in arrays of vacuum microdiodes," Plasma Sciences (ICOPS) held with 2014 IEEE International Conference on High-Power Particle Beams (BEAMS), 2014 IEEE 41st International Conference on , vol., no., pp.1,1, 25-29 May 2014

- Ilkov, M.; Torfason, K.; Manolescu, A.; Valfells, Á , "Thermal effects in microdiode bunching," Plasma Sciences (ICOPS), 2015 IEEE, 24-28 May 2015

- Ilkov, M., "Synchronization of vacuum microdiodes", talk, Lecture Marathon, Reykjavik University Lecture Marathon, 28 March 2014

- Ilkov,M., "Electron bunching and synchronization in microdiodes", talk, Institute of Physics and Astronomy, Potsdam University, 13 December 2013

- Ilkov, M.; Torfason, K.; Manolescu, A.; Valfells, Á , "Vacuum microdiodes as possible sources of THz Radiation", COST Meeting and SMMO14 conference, Marburg 27 February -1 March 2014

- Ilkov, M.; Torfason, K.; Manolescu, A.; Valfells, Á ,"Vacuum microdiodes as possible sources of THz radiation", Sheffield 10-11 Oct. 2013

---

[1]Underlined name in all these references is the presenter

Contents

List of Figures

List of Tables

Chapter 1

Introduction

Progress of science is unequivocally bound to progress in instrumentation. Whether it is spectroscopy, communication, imaging or just pure physics, terahertz (THz) radiation promises a big leap forward. This thesis is concerned with space-charge dynamics, primarily with regard to generation of THz modulated beams.

Terahertz (1THz=10^{12}Hz) radiation is an active field of research with applications in communications, security screenings, molecular spectroscopy, medicine, and deep-space research, to name a few examples [1], [2], [3], [4], [5], [6], [7], [8], [9]. Although there is no unique definition for the term Terahertz radiation, it is commonly used to refer to the frequency range from ∼100GHz (1GHz=10^{9}Hz) to ∼10THz [1]. It is also called submillimeter radiation as the wavelengths range from ∼1mm to ∼0.1mm. Terahertz radiation is non-invasive, non-destructive and intrinsically safe. This makes it such a desirable and new field that researchers around the globe are racing to find a practical source for it. Although producing and detecting coherent terahertz radiation remains a major problem, the lower part of the spectrum from 100GHz to 1000GHz is covered by inexpensive devices like gyrotrons, backward-wave oscillators and resonant- diodes [10].

Terahertz is found between microwave (MW) and far-infrared radiation (FIR). It shares some of the properties of both. Producing and measuring THz radiation is a problem for solid state devices. At such frequency, the junction transit time is too long and transistors and other devices based on electron transport can work in principle up to frequencies of 300GHz but in practice this limit is 50GHz. On the other hand, optical devices can produce frequencies down to 30THz [11], [12], [5].

Figure 1.1: Electromagnetic spectrum and the terahertz gap [11]

Some of the applications of terahertz radiation follow.

Use of THz radiation in the pharmaceutical industry can be found in inspection of tablet integrity. Although there are ways of identifying faults in the tablet coating, these faults are found after a batch is produced. A sample is taken and tested (usually destructively). With THz imaging, this can be done real-time on-site. This can significantly cut production losses [10].

THz spectroscopy is sensitive to inter- and intra-molecular vibrations and can be used as means for molecular spectroscopy. With pulsed terahertz imaging, the 3D structure and the folding process of proteins can be explored [13]. THz spectroscopy can reveal fast protein kinetics in the femto-second time frame by showing the rearrangement of protein structure.

In the cosmetic industry, the moisturization of the skin (retention of water in the stratum corneum) is of vital importance. THz radiation is strongly attenuated in water and can thus be used to measure levels of water in the skin.

In dermatology, Basal Cell Carcinoma (BCC) is the most common form of skin cancer worldwide in white population [14]. Terahertz pulse imaging (TPI) is a non-invasive technique from this frequency region. The wavelength of THz radiation is much larger than the tissue structures and thus it is negligibly scattered [15]. With TPI, both amplitude and phase can be obtained from which absorption and refractive index can be inferred. TPI may be able to show type and 3D image of such tumors.

In dentistry, if decay is detected early enough, drilling into the cavities becomes unnecessary as fissure sealing and remineralization can fix the problem. THz imaging can distinguish between different kinds of tissue thus exposing the early stage cavity [10].

1.1   Sources of THz radiation

It has by now become obvious that the development of practical, table-top room-temperature, devices for production and measurement of THz radiation is of paramount importance. There are a couple of main streams through which the scientific community is trying to achieve the aforementioned goals.

1.1.1   Optical Sources

Among the most successful THz sources are quantum-cascade lasers (QCL) [5],[7]. QCL have some limitations however. They must be cryogenically cooled and are limited to producing 100's of milliwatts of THz radiation. Representative parameters show a frequency range of 0.84 - 5.0 THz, a maximum operating temperature of 169 K for pulsed radiation and 117 K for continuous wave (CW), while maximum power is 250 mW for pulsed and 130 mW for CW radiation [7].

1.1.2   Vacuum Electronic Devices (VED)

Vacuum microelectronic devices or in some sources free electron based sources, can be used as sources of gigahertz or even terahertz radiation. Examples of such devices used are microtriodes [16],[17], nanoklystrons [18] and travelling wave tubes [19]. Most of these devices rely upon field emission for their operation, although photoemission could be used for cold cathode emission. For electrons emitted from metal surfaces into free space, the current emitted at the low current regime is said to be source-limited. Such emission can be divided into three groups, namely, thermionic emission, photo-emission and field emission. These three emission mechanism are described by the Richardson-Laue-Dushman (RLD) law [20],

the Fowler-Nordheim (FN) law [21] and the Fowler-Dubridge (FD) law [22],[23],[24]. An overview of the three is given by Jensen [25] and also a generalized emission model for the three emission mechanisms [26]. The other regime is the source-unlimited where space charge effects come forwards. Space-charge limited flow in a diode has been a subject of investigation for over a century. Nonetheless this field of research remains quite fertile in terms of interesting results. The past fifteen years have seen considerable work on extending the classical Child-Langmuir law [27], e.g. for very small structures [28], [29], [30]; finite emitter area and pulse length [31], [32], [33]; space-charge limited field emission [34], [35],[36]; as well as development of novel scaling laws and investigations into the nature of space-charge limited flow [37], [38], [39], [40].

Due to the inherent superiority of VED to solid state devices for producing high-power at high frequency [41],[42] it is natural to pursue that avenue in search of efficient, high-power THz sources. However, it should be noted that the high power VED devices are both extremely large and expensive [3],[4]. Nonetheless, with the advent of modern manufacturing techniques there is the promise of devising compact VED THz sources that are superior to solid state devices and QCL [4], [41], [43], [44], [19], [45].

Recent simulations of nanoscale vacuum diodes have indicated a mechanism for bunching of the beam from the cathode with a frequency corresponding to THz [46]. The mechanism is based upon copious photoemission from a cold cathode, where the injected current is much greater than the space charge limit [47], [32],[30],[31],[27], [38]. Electrons are emitted from the cathode at a high rate until their density is such that they inhibit further emission. As this bunch of electrons is accelerated away from the cathode the effect of its space-charge field at the cathode diminishes to a point where the orientation of the surface field at the cathode becomes favorable and emission resumes, resulting in the formation of a new bunch. Similar results were observed experimentally [48].

For suitable diode dimensions (of the order of 1 μm), emitter area (scale length on the order of 100 nm), and potential difference applied to the diode (the order of 1V) it is possible to generate a continuous stream of electron bunches which arrive at the anode with intervals corresponding to THz frequency. The frequency is determined by the vacuum electric field in the diode, and the radius of the emitting area on the cathode [49]. This mechanism is a many-electron version of the well known Coulomb blockade familiar in single electron transport in nanosystems. The THz oscillation has, in fact, been shown to occur for Coulomb blockade in single electron emitters [40].

1.2   The Child-Langmuir Law

As the current grows in a diode, space charge effects become more important. The charge in front of the cathode creates a field opposing further emission of electrons. This is known as space-charge limited (SCL) regime where the current drawn from an emitter is the maximum possible to be transported across in a steady state one-dimensional (1D) gap. For such a 1D gap of spacing, D, and dc voltage across it, V, the 1D classical Child-Langmuir law is

$$I = \frac{4\epsilon_0}{9} \sqrt{\frac{2e}{m}} \frac{V^{3/2}}{D^2} \tag{1.1}$$

where ϵ_0 is the vacuum permittivity, e is the electron charge and m is the electron mass. We will first derive the Child-Langmuir Limit. The kinetic energy of an electron would be

$$\frac{1}{2}mv^2 = eV \tag{1.2}$$
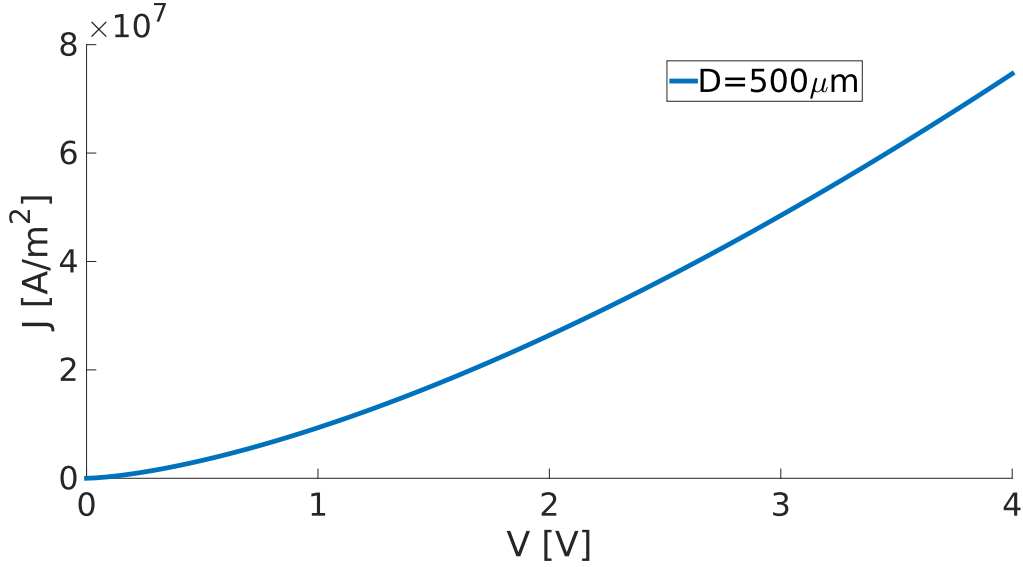
Figure 1.2: The Child-Langmuir law for a representative set of parameters: D up to $500\ \mu m$ and $V = 4$ V

where v is the electrons speed and the current is $I = \rho v$, ρ being the charge density. Finally the Poisson equation states

$$\nabla^2 V = \frac{\rho}{\epsilon_0} \tag{1.3}$$

From 1.2 we get $v = \sqrt{2eV/m}$ and from conservation of current follows $\rho = I/v = I\sqrt{m/2eV}$. In the 1D case, 1.3 becomes

$$\frac{d^2 V}{dx^2} = \frac{\rho}{\epsilon_0} \tag{1.4}$$

Using

$$d\left(\frac{dV}{dx}\right)^2 = 2\frac{dV}{dx}\frac{d^2 V}{dx^2}dx \tag{1.5}$$

We get

$$d\left(\frac{dV}{dx}\right)^2 = 2\frac{d^2 V}{dx^2}dV = 2\frac{\rho}{\epsilon_0}dV = 2\frac{I}{\epsilon_0}\sqrt{\frac{m}{2eV}}dV \tag{1.6}$$

After integration

$$\left(\frac{dV}{dx}\right)^2 = \frac{4I}{\epsilon_0\sqrt{2e/m}}V^{1/2} \tag{1.7}$$

One more integration where for x we integrate from 0 to D (the gap spacing) we get the well known Child-Langmuir Law

$$I = \frac{4\epsilon_0}{9}\sqrt{\frac{2e}{m}}\frac{V^{3/2}}{D^2} \tag{1.8}$$

For one of the most used variable configurations in this thesis, D up to $500\ \mu$m and $V = 4$ V, the space-charge limited current density looks like Fig. 1.2

The analysis of the Child-Langmuir law has been extended to include two-dimensional (2D) geometry [32] , quantum effects [50], the Coulomb blockade regime [30], limited emission area [51], [32] and finite pulse length [31]. These improvements have been done to

explore the onset of space-charge limited current while our work has been mostly after this regime has been established.

Chapter 2

Computational Methodology

This PhD project shows the work done on investigating a possible THz radiation source through simulations. The source is meant to be with size of the order of $< 1\mu$m. Such a device would operate with a small number of electrons ($n_e \sim 1000e^-$). The electron bunching mechanism through which THz modulated beams are created is explained in detail in chapter 3. In this chapter we present the two most common simulation methods in the plasma physics community and we explain why we chose to use the molecular dynamics method.

2.1 Particle-in-Cell (PIC) methodology

The physical representation of the material world consists of evaluating the interaction between matter elements through force fields. Such interaction can be represented, and outcomes calculated, through simulations done on a computer. One way of such representation is the Particle-In-Cell (PIC) method. This method is used frequently by the plasma physics community due to its ability to simulate systems consisting of very large number of particles.

If we label each particle with a number i, then its position will be x_i and its velocity v_i. There are 2n variables for n dimensions, so in our case 6 variables for 3D system. These property variables are enough to calculate the force exerted on the particle.

$$\boldsymbol{F}_i = q_i \boldsymbol{E}_i(\boldsymbol{x}_i) + \boldsymbol{v}_i \times \boldsymbol{B}_i(\boldsymbol{x}_i) \tag{2.1}$$

Naturally, q is the particle charge and $\boldsymbol{E}_i(\boldsymbol{x}_i)$ and $\boldsymbol{B}_i(\boldsymbol{x}_i)$ are the electric and magnetic fields at the particle's position respectively. The fields are calculated through Maxwell's equations.

$$
\begin{aligned}
\nabla \cdot \boldsymbol{E} &= \frac{\rho}{\epsilon_0} \\
\nabla \cdot \boldsymbol{B} &= 0 \\
\nabla \times \boldsymbol{E} &= -\frac{\partial \boldsymbol{B}}{\partial t} \\
\nabla \times \boldsymbol{B} &= \mu_0 \boldsymbol{J} + \mu_0 \epsilon_0 \frac{\partial \boldsymbol{E}}{\partial t}
\end{aligned}
\tag{2.2}
$$

If we consider a system with very few particles, a test particle will be affected by the overall mean field from all the other particles, but its movement will be mostly due to close proximity interactions with other single particles. Only close particles have effect since the forces decay very fast with increasing distance. This will create a jumpy trajectory of the test particle and this system is called *strongly coupled*.

The opposite situation occurs when the number of particles in the system is large and the test particle is found in virtually continuous environment of other charges. It's trajectory will be smooth. This is called *weakly coupled* system.

To put it in more concise form, N_D is the number of particles in a box with a side of Debye length, λ_D and the density of particles in the box is n.

$$N_D = n\lambda_D \tag{2.3}$$

Each particle occupies space $V_i = n^{-1}$ and from here the average inter particle distance can be calculated as $a = V_i^{1/3}$. The *potential* electrostatic energy for a particle can be calculated as $E_{pot} = \frac{q^2}{4\pi\epsilon_0 a}$ and the *kinetic* thermal energy is in the order of $E_{th} = k_B T$, where k_B is the Boltzmann constant. Debye length is $\lambda_D = \sqrt{\frac{\epsilon_0 k_B T}{ne^2}}$ and so, the plasma coupling parameter, Λ we define as

$$\Lambda = \frac{E_{th}}{E_{pot}} = \frac{4\pi\epsilon_0 k_B T}{q^2 n^{1/3}} = 4\pi N_D^{1/3} \tag{2.4}$$

This relation shines new light on the weakly and strongly coupled systems' definitions. If the number of particles in a Debye box is very large the thermal energy exceeds by far the potential energy and Λ is large, thus the system is weakly coupled. On the other side, if the number of particles in the Debye box is small, the potential energy is larger than the thermal energy, Λ is small and we are talking about a strongly coupled system.

For simulation of weakly coupled systems collective clouds of particles are used instead of single particles. This can reduce the number of simulated particles greatly, yet realistically simulate the behavior of a large number of real particles. Although these clouds are collective entities, the charge to mass ratio stays the same as in individual particles. When two clouds are far away they interact through Coulomb interaction as any two individual particles would (fig 2.1a). As they start to overlap, the overlapping region gets neutralized (fig 2.1b) thus eliminating a key element that is very important to us - collisions.

(a)   (b)
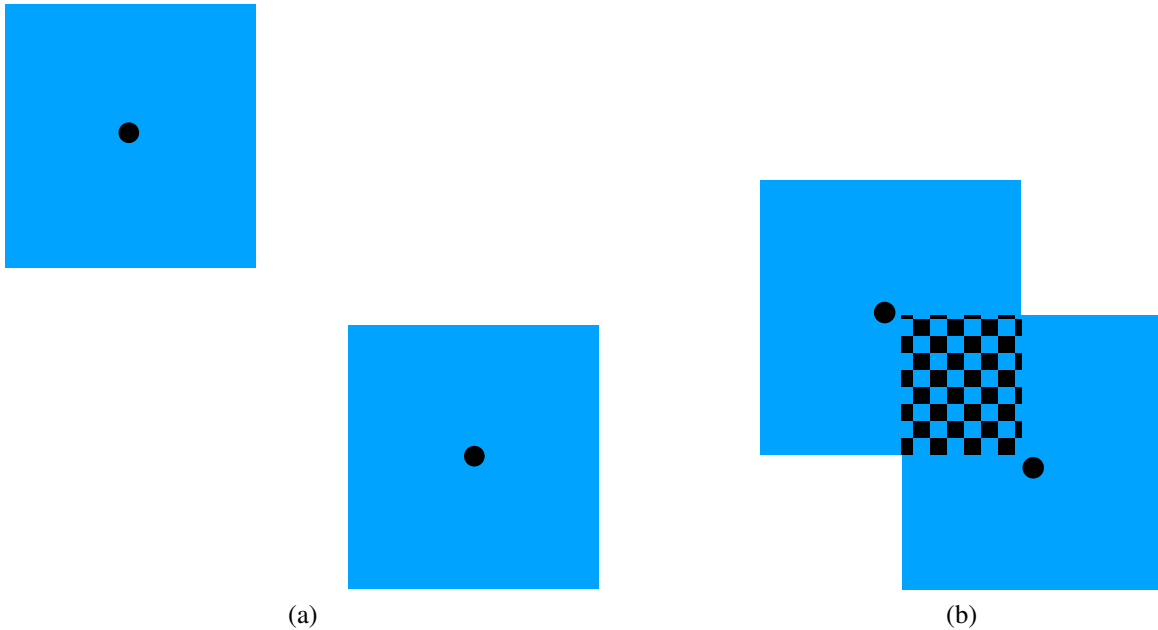
Figure 2.1: PIC squares before and after overlap. Checkered area represents the overlap.

This same statement can be seen in fig. 2.2. There it can be seen that as the elements are far away, the weakly and strongly coupled simulated systems act the same and the force

between them is the same. As they start to come closer together, the particle-particle interaction force grows into singularity, while the cloud-cloud force starts to decrease and reaches zero at perfect overlap.
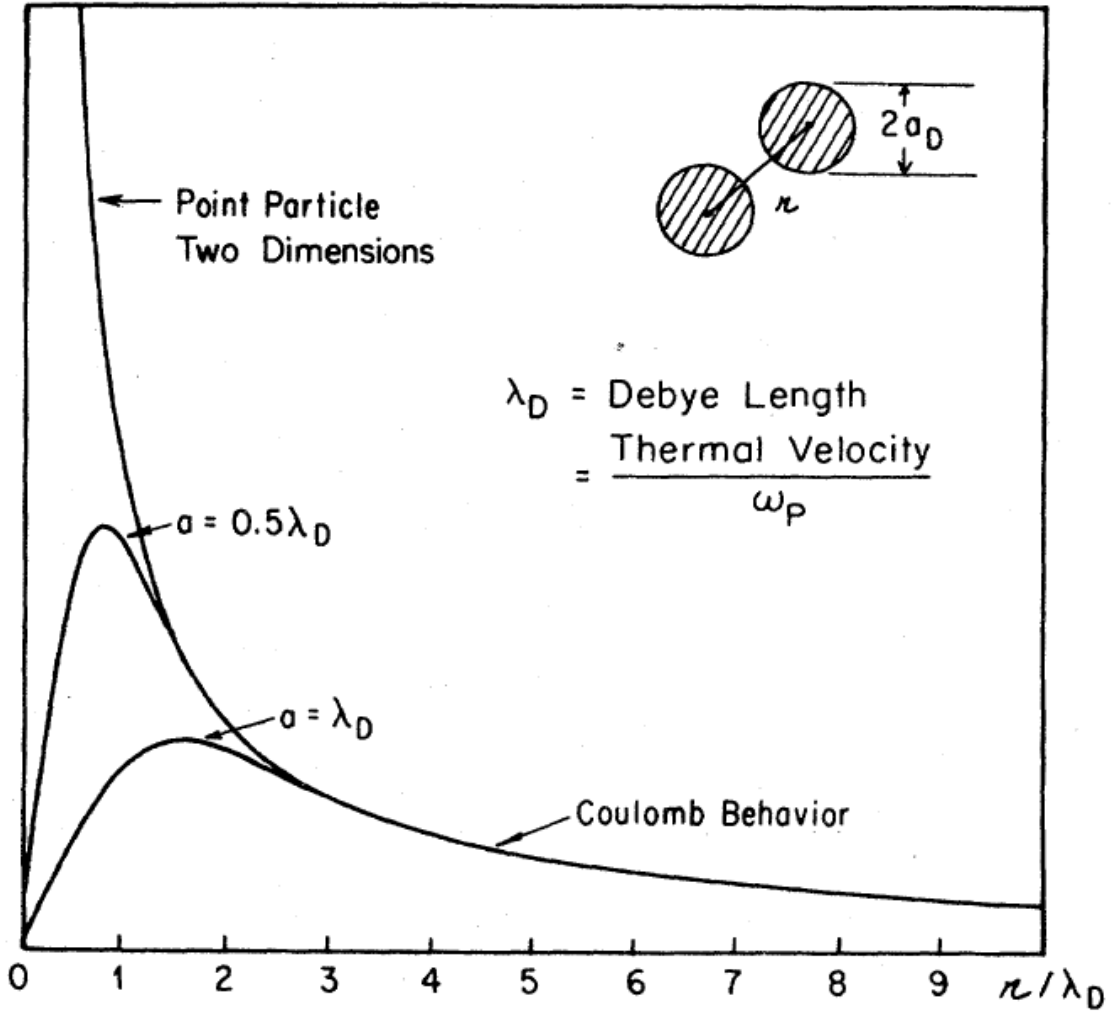
Figure 2.2: PIC versus MD as given in Dawson (1983) [52]

2.2 Molecular Dynamics (MD) methodology

The molecular dynamics method uses the particle-particle interaction to calculate the force between each and every one of the particles. It is a numerical scheme to solve the fundamental Newton's equations of motion. This method is computationally very expensive as the number of computations rises with $\mathcal{O}(n^2)$, but on the other hand this method gives results with higher fidelity and most importantly for us - collisions are included. One other reason why we chose to use the MD over PIC was the fact that our system contains in the order of hundreds of electrons, which, although requires long computational times, is obtainable. MD simulations are being used in many atomic and molecular systems, in solid state physics, biology, plasma physics etc.

2.3   Particulars of our MD simulation

The system under study is a parallel plate vacuum microdiode of infinite area. However, electrons are only emitted from a circular disk on the surface of the cathode with the radius R_E. In a Cartesian coordinate system the normal direction on the cathode and on the anode is the z axis, the two electrodes being located at $z = 0$ and $z = D$ respectively. Note that D is also the gap spacing. It is assumed that there is an infinite supply of electrons present inside the cathode, beneath the cathode-vacuum interface, ready to be injected into the gap if the surface electric field is favorable (i. e. with a negative z component, leading to acceleration of the electrons away from the cathode, towards the anode). Thus, emission can never be source-limited. Furthermore,in the initial investigations it was assumed that the electrons are emitted with negligible velocity and that they are point-like. The dynamical behavior of the electrons is obtained by applying the molecular-dynamics method. The repulsive interactions between electrons present in the gap are modeled using an exact Coloumb potential for point charges. To drive the electrons from the cathode to the anode an external field is applied by setting the potential across the diode as V_g. The time is discretized in small intervals Δt. An iteration in the simulation is carried out in three stages: A) Emission, B) Particle advancement and C) Absorption. We will now describe each component briefly.

2.3.1   Emission

If not otherwise stated, all and any emission processes described in this thesis, up to chapter 5 are performed with zero initial velocity, $v_0 = 0$. Particle emission is carried out using a Monte Carlo approach. In each time-step electrons are injected at random positions on the cathode surface. The injection is automatically suppressed when space-charge limited conditions are reached, namely when there is no spot on the cathode where the total electric field (which is the sum of the field created by the applied voltage and of the field created by the electrons present in the gap) is oriented in the negative z direction, so that it cannot transfer more electrons into the gap. The computational method is the following: A random point, $p_1 = (x_1, y_1, 0)$, on the surface of the cathode within the emitter region $x^2 + y^2 < R_E^2$ is selected. To determine if this point is blocked by the present space-charge distribution a test is done. This test relies on the z-component of the accelerating field calculated at a point, $p_{1\alpha} = (x_1, y_1, -h/2)$, immediately below p_1, by adding the contribution from the applied vacuum field and the field from each of the N electrons already present in the diode gap. If the electric field at $p_{1\alpha}$ is favorable, then an electron is placed at the point, $p_{1\alpha} = (x_1, y_1, h/2)$, which is directly above $p_{1\alpha}$ but separated by a distance of h. Thus the number of electrons in the gap becomes $N + 1$. In our simulations we give h the value of 2nm. The implications of picking this value will be discussed later. If the field at $p_{1\alpha}$ is not favorable then no placement of an electron occurs and a failure of injection is registered. The next step is to pick another point, $p_2 = (x_2, y_2, 0)$, in the same random manner. Subsequently, the z-component of the electric field is calculated at $p_{2\alpha} = (x_2, y_2, -h/2)$. If the field is favorable for emission at that point an electron is placed at $p_{2\beta} = (x_2, y_2, h/2)$, the number of electrons in the gap is increased by one, and we carry on picking points of emission at random. Similarly, if the field is unfavorable we place no electron, register a failure of injection and move on to pick another point. However, if there is a failure to inject in 100 consecutive attempts, we deem that space-charge limited conditions have been reached and cease trying to place more electrons. At this juncture the simulation moves on to the next step which is particle advancement.

2.3.2 Advancement

At a given time, $t = t_i = i \times \Delta t$, there are N_e particles in the gap. Here Δt is the time step, which is equal to 1fs in our simulations. The position of a particle at this time is given by $r_{ni} = (x_{ni}, y_{ni}, z_{ni})$, where n ranges from 1 to N_e. The force acting upon the particle at this time is $F_{ni} = (F_{xni}, F_{yni}, F_{zni})$, and is the sum of the force due to the applied vacuum field and the respective electrostatic force between electron n and all the other $N_e - 1$ electrons as calculated from their positions at time t_i. We then determine the location for that particle at time $t_i + 1 = t_i + \Delta t$ using the Störmer-Verlet method [53], [54], [55]

$$x_{n(i+1)} = 2x_{ni} - x_{n(i-1)} + \frac{F_{xni}}{m}(\Delta t)^2 \qquad (2.5)$$

where m is the mass of the electron. The same method is used to calculate $y_{n(i+1)}$ and $z_{n(i+1)}$. For the electrons injected at time t_i there is no defined position at time t_{i-1} and in this case we use:

$$x_{n(i+1)} = x_{ni} + \frac{F_{xni}}{2m}(\Delta t)^2 \qquad (2.6)$$

The position of electrons are calculated in this manner as long as they are in the gap. Once they cross the x-y plane at either $z = 0$ or $z = D$, corresponding to the cathode and anode respectively, they are removed from the simulation. It is thus possible that a recently injected electron is pushed back into the cathode due to the evolving electrostatic field created by the space-charge distribution. This kind of event is however rare, the regular case being the propagation towards the anode.

2.3.3 Absorption

For the purpose of this study, the interest lies in examining the number of electrons emitted from the cathode and absorbed by the anode as a function of time. At each time step the number of particles emitted at the cathode and absorbed at the anode is recorded. The frequency of absorption at the cathode is negligible compared to emission and absorption at the anode. Due to the discrete time step there is an inherent graininess in the absorption profile. In addition there is also the question of the immediacy of electron absorption, i.e. how well one may specify when an electron is absorbed. Consider an electron at the anode. Its kinetic energy is equal to the applied potential, and the corresponding deBroglie length is given by

$$\lambda_e = \frac{h}{\sqrt{2meV_g}} \qquad (2.7)$$

where h is Planck's constant, m the mass of the electron as before, e the elementary charge and V_g the applied potential. Near the anode, the velocity of the electron is close to its terminal velocity and one can easily estimate the time that it takes an electron, drifting at this velocity, to travel one deBroglie length. Let us call that time, t_e, then we have:

$$t_e = \frac{h}{2eV_g} \qquad (2.8)$$

For instance, if $V_g = 1$V we have $t_e \approx 2$fs. To alleviate the discrete character of the simulation we incorporate a procedure after gathering the absorption data, whereby the charge of each electron is spread through time using a Gaussian filter. To wit, if $T = [T1, ..., TP]$ is a record of all the times an absorption event takes place in a given run of the simulation, then

the Gaussian filter is applied to give a continuous function $I(t)$ which describes the current at the anode at any time:

$$I(t) = \frac{e}{\sqrt{2\pi}\sigma} \sum_{k=1}^{p} \exp\left[-\left(t - T_k\right)^2 / 2\sigma^2\right] \tag{2.9}$$

where σ is the width of the filter and has units of time. In other words, this is convolution of the signal with a Gaussian. The same type of smoothing can be used to define a continuous current at the cathode. For the purpose of analysis the width of the filter should be picked so that $t_e < \sigma << T$, where T is a characteristic time describing the interval between bunches in the beam. A larger value of σ yields smoother current profiles and will also act as a high frequency filter in spectral analysis.

Chapter 3

Electron Beam Bunching

Initially, computer simulations were performed with zero initial velocity to explore the effects of the vacuum field E_g on the frequency of the emitted current. Later on, we expanded our inquiry onto multiple diodes and synchronization, as well as including non zero initial velocity of the electrons. Firstly, we start with the bunching and frequency dependence on the electric field.

3.1   Bunched current formation theory

In order to explain how the current in our diodes (Fig. 3.1) gets longitudinally modulated we will use the paper by Pedersen et al. [46] which covers this subject extensively.
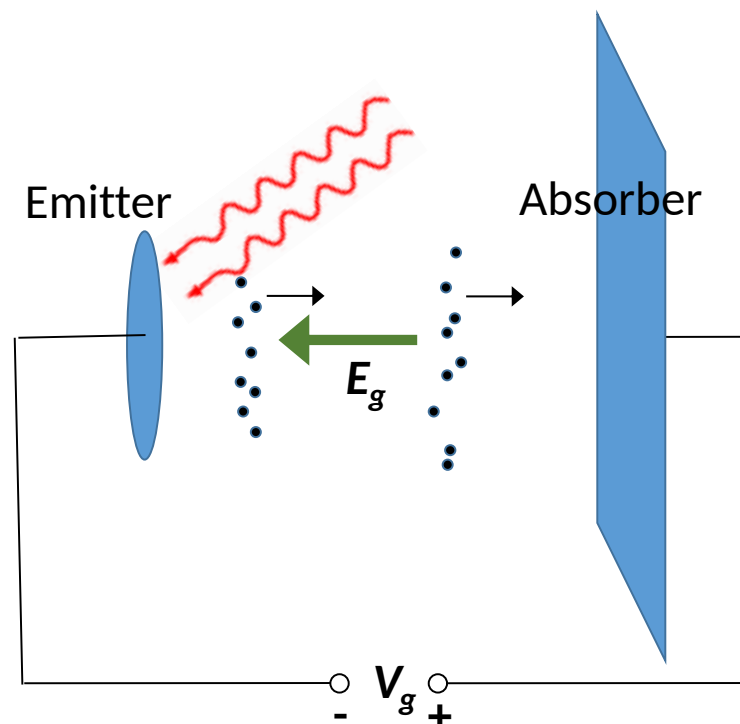

Figure 3.1: The device is a vacuum diode with a disk-shaped emitter on an infinite cathode under a strong laser pulse. The electrons are extracted in bunches and are driven to the absorber (anode) by the electric field E.

The During one period of emission oscillation , the cathode goes through three phases: (1A) Creation of charge sheet, which is basically an imagined 2D distribution of electrons, (1B) Blockade of the cathode once the charge sheet has been fully created and (2) Reopening of the cathode for further emission. Throughout this process the electric field is calculated at every point on the emitter, namely, $E_{tot,z} = E_g - E_{sc,z}$. Here $E_{tot,z}$ is the z-field calculated at the emitter, E_g is the vacuum field created by the potential difference between the anode and cathode and $E_{sc,z}$ is the collective space-charge electric z-field. The process is shown in fig. 3.2. Once an electron is emitted, it is placed immediately after the cathode and thus it's z-component of the field has an area limited only in its closest proximity as in fig. 3.2-1A. This area is not affected by all the other electrons yet. When the charge sheet is fully formed, and the surface of the cathode is fully covered, electron emission stops (see fig. 3.2-1B). As the charge sheet starts moving towards the anode, the influence region of each electron increases because it depends not only on the distance of an electron from the emitter, but also from the angle between the point in question on the emitter and the electron. The further the charge sheet is, the electric field on the cathode starts to change from discrete to continuous. Once a critical distance is covered, the cathode reopens for emission, fig 3.2-2. A new charge sheet is formed and the whole process starts again. A simple toy model analytical solution for these oscillations follows. A charge sheet of radius R is created and it is accelerated by an external field E_g. It's distance from the cathode is denoted by z. The field created in the center of the cathode due to the sheet will simply be

$$E_{sc,z} = E_0 \left(1 - \frac{z}{\sqrt{z^2 + R^2}} \right) \tag{3.1}$$

where $E_0 = \sigma/2\epsilon_0$ and $\sigma = -Ne/\pi R^2$ is the charge density created by a sheet of N uniformly distributed electrons, assuming homogeneity and continuous distribution of charge. For the z-component of the total field to become zero in the center of the cathode, the sheet needs to have traveled a distance of

$$z_0 = R \frac{(1 - E_g/E_0)}{\sqrt{1 - (1 - E_g/E_0)^2}} \tag{3.2}$$

Under the assumption that the acceleration $a = eE_g/m$ is constant, m being the electron mass, then the time until $E_{sc,z}$ reaches zero will be $t_0 = \sqrt{2mz_0/eE_g}$. The frequency is simply $f = 1/t_0$:

$$f = \sqrt{\frac{eE_g}{2mR}} \frac{\left[1 - (1 - E_g/E_0)^2 \right]^{1/4}}{(1 - E_g/E_0)^{1/2}} \tag{3.3}$$

3.2   Bunched current simulation results

To explore the effects of the vacuum field E_g, simulations were run for 64 combinations of applied potential and gap size, with a fixed circular emitting area of 250 nm radius. The values for the potential applied were $V_g = [0.5, 1.0, 1.5, 2.0, 2.5, 3.0, 3.5, 4.0]$ V and the values for the gap size were $D = [0.5, 1.0, 1.5, 2.0, 2.5, 3.0, 3.5, 4.0]\mu$m. Furthermore, 14 combinations of V_g and D were inspected for an emitter area with a radius of 100 nm, and for 6 combinations of V_g and D when the emitter radius was decreased to 50 nm. The choice of parameters was based on our previous work where a gap spacing of 1 μm and applied
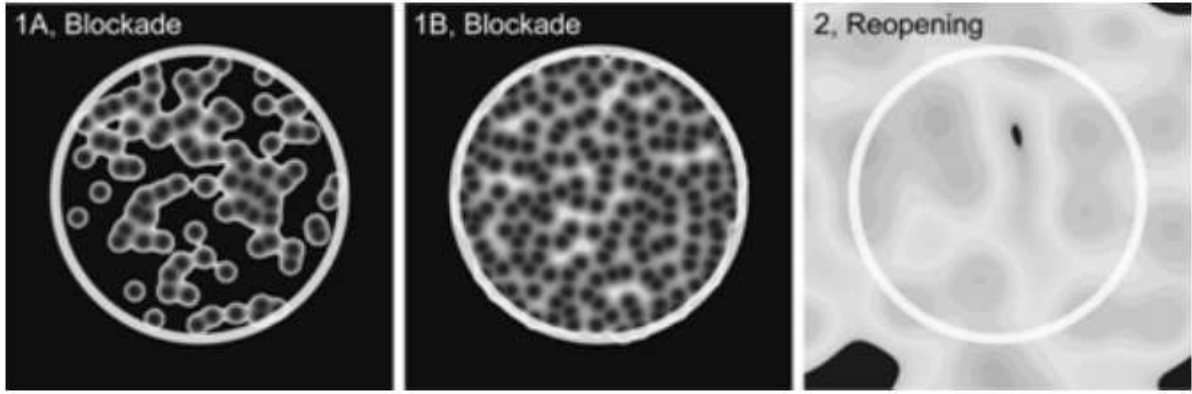
Figure 3.2: Diode Opening (taken from [46])

potential of 1 V with an emitter radius of 250 nm gave a frequency around 0.8 THz, indicating that this was the regime of interest. Since this type of modulation does not appear in large diodes we restricted our investigation to gaps smaller than 4 μm. For each combi-
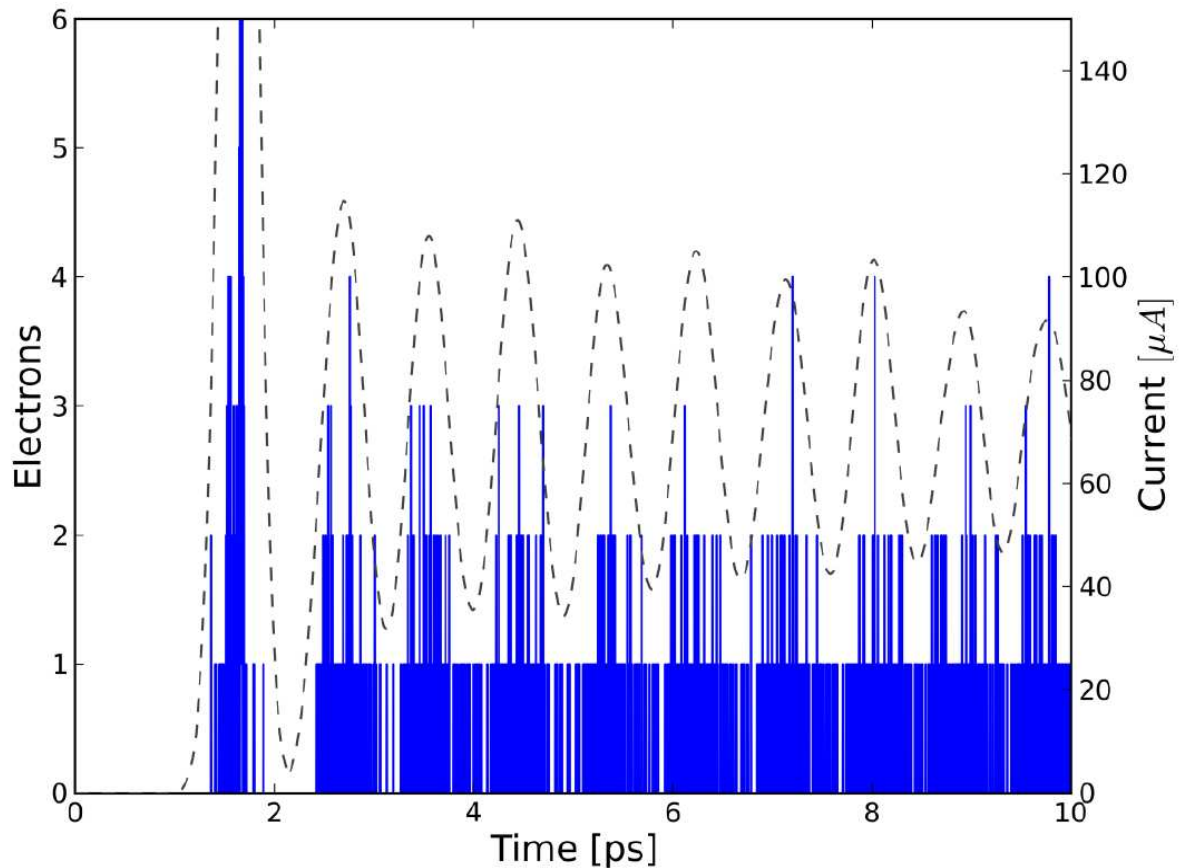
Figure 3.3: Comparison of raw data showing number of electrons absorbed at anode per iteration and current at anode obtained using Gaussian filter (dashed line). Gap spacing is $D = 500$ nm and applied voltage of 1 V, while the Gaussian smoothing filter uses = 150 fs and emitter radius is $R = 250$ nm.

nation, time series recording the number of electrons emitted at the cathode and absorbed

at the anode were generated. Fourier analysis was carried out for both the raw time-series and also for the conduction current at the electrodes determined by the above described Gaussian filtering. From the resulting spectra the dominant frequency as well as the full-
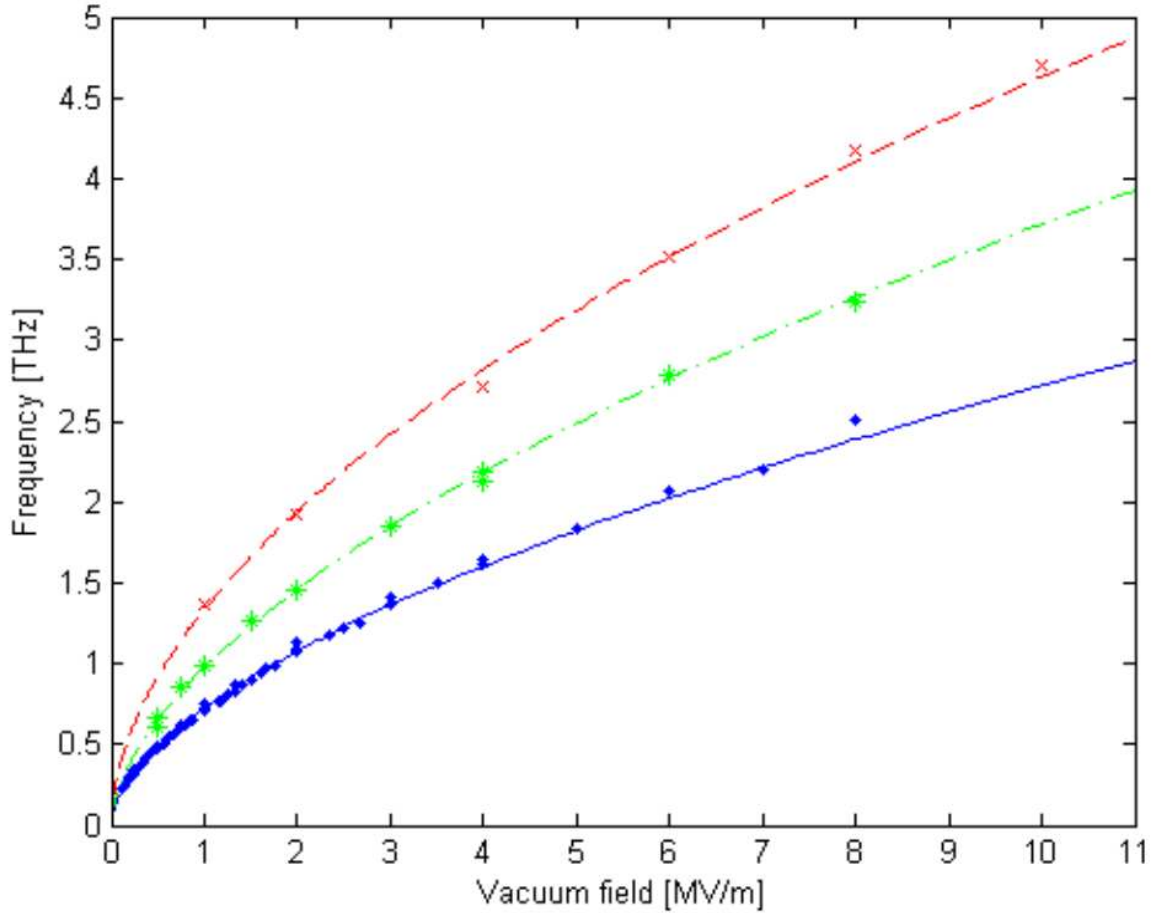
Figure 3.4: Modulation frequency of the steady state current at the anode as a function of applied vacuum field shown for 84 different combinations of gap size, applied potential and emitter size. The solid line represents the frequency as described by Equation 5.3 fitted to the data (dots) for $R_E = 250$ nm. The dash-dotted line represents the fitted to the data (stars) for $R_E = 100$ nm. The dashed line represents the fitted to the data (crosses) for $R_E = 50$ nm.

width-at-half-maximum (FWHM) of the corresponding spectral peak are defined and have been determined. Figure 3.5. shows the frequency spectrum for the anode current in the case of an applied voltage $V_g = 1$ V and gap spacing of $D = 0.5\mu$m for both unfiltered and filtered data. As can be seen, the filtering process removes some of the high-frequency components, but does not alter the main bunching frequency. We find that the dominant frequency, which describes the bunching, is a simple function of the applied electric field. This can be seen clearly in Figure 3.4. In fact, the relation between the frequency and the applied field can be described by a simple power law:

$$f = A \times E^\alpha \tag{3.4}$$

where f is the frequency measured in Hz, and E is the applied vacuum field measured in V/m. The parameters A and α depend upon the size of the emitter, i.e. the radius of the
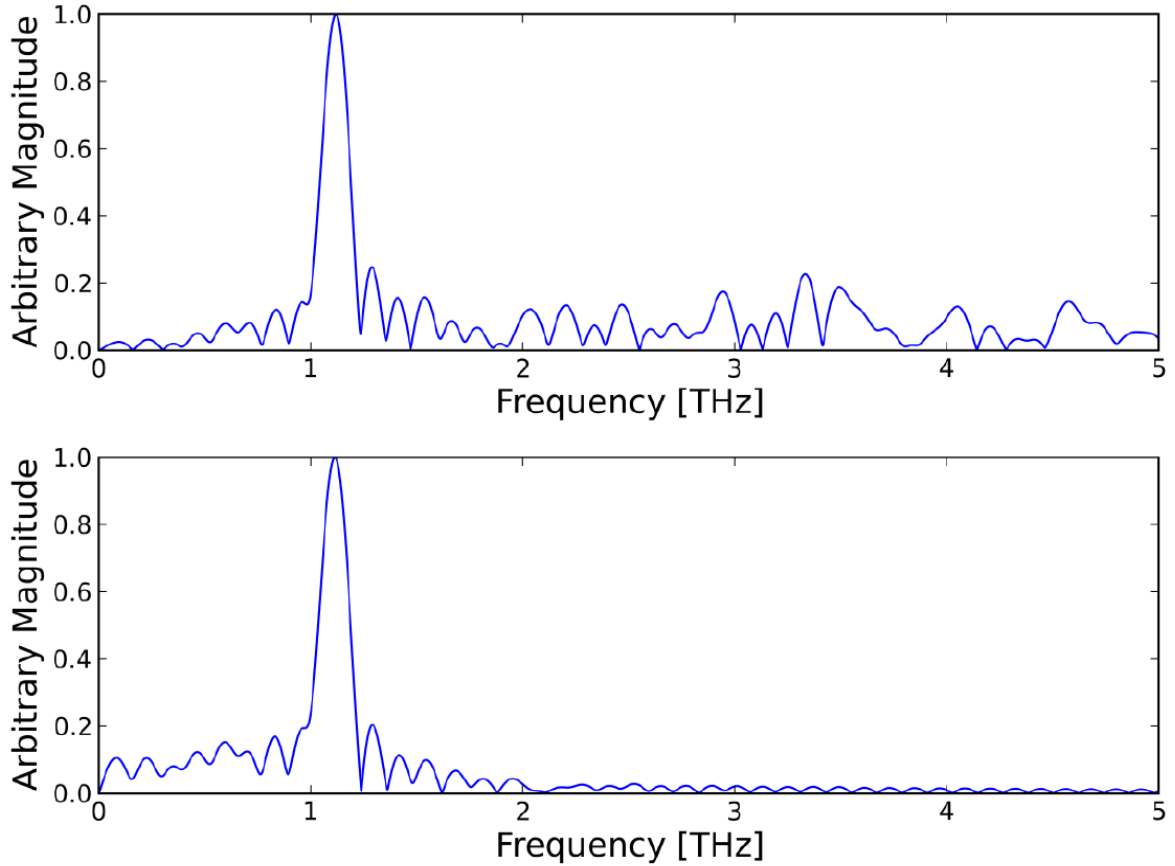
Figure 3.5: Spectrum of raw data for electron absorption at anode (upper) and anode current obtained using Gaussian filter (lower). The same parameters are used as in Figure 3.3.

circular are of emission on the cathode. Table 3.1 shows the values of the parameters A and α for three inspected emitter radii.

Emitter radius [nm]	A	α
50	779×10^6	0.539
100	326×10^6	0.580
250	257×10^6	0.575

Table 3.1: Magnitude of the parameters in Eq.3.4, $f = A \times E^\alpha$, for different values of the radius of the emitting area

However, the width of the corresponding spectral peak is not so simply dependent on the applied field. The normalized FWHM, defined as the FWHM of the peak divided by the peak frequency, ranges from about 0.1 to 0.3, and is noticeably dependent on both the applied potential and gap size, rather than being dependent solely on the applied field. We come back to that in the final part on nonzero initial velocities where peak structure is looked into more detail.

The relation given in equation 5.3 shows a different scaling between frequency and field strength from the $E^{3/4}$ scaling predicted by the toy model that was originally used to explain the origin of space-charge modulation observed in the microdiode [46]. This difference can be explained qualitatively by noting that in the toy model a rigid disk shape was used to describe the bunches parallel to the emission plane, and more importantly only a single bunch was assumed to be present in the diode gap at any time. With more than one bunch in the gap, the trailing bunch(es) will be expected to experience a weaker accelerating field and therefore a longer time to travel the sufficient distance from the cathode so that it may reopen for emission. This results in a longer interval between emission cascades and, thus in a lower frequency. The toy model also indicates that the frequency should rise with diminishing emitter radius. This effect can be seen clearly in Figure 3.4. The simple power law relation between the frequency and applied electric field, for fixed emitter areas, is a new and useful result, as it implies that a microdiode could be used as an easily tunable oscillator, and gives a quantitative means of predicting the frequency. Also, by selecting an appropriate radius for the emitter area it is possible to set the frequency range available for a given range of applied electric field strength.

Chapter 4

Diode Arrays

Because until now, the modulation of the electron beams under investigation are persistent and easily tunable in the THz range, simply by varying the DC potential applied to the diode, it is tempting to examine the possibility of using it as a practical THz generator, either directly radiating or as a bunched electron source for a compact vacuum electronic amplifier. However, the current from such a microdiode is typically around tens of microamperes for an applied potential around 1V [49]. Thus, the expected power output from a single diode would be quite small. Increasing the emitter area is not a satisfactory option to increase the output power as the bunching frequency decreases, and the quality of the bunches degrades with increasing emitter radius [49]. These considerations suggest the possibility of synchronizing an array of emitters in order to generate a coherent signal of increased power and THz frequency. In general, synchronization means adjustment of rhythms in self-sustained periodic oscillators due to their weak interaction [56]. If two oscillators with the same frequency synchronize, their instantaneous phase difference is zero. This would lead to strengthening of the signal and increase power output. However, the individual frequencies are expected to drop due to the interaction. Now we will look into the interaction of electron bunches from emitter arrays for evidence of synchronization and understanding of the physical principle behind it.

4.1   System model and simulation method

The system under consideration will be the same as before: cathode with $R_E = 150$nm, infinite anode and gap spacing of $D = 500$nm and voltage between them of $V_g = 4$V. Before or after, if not otherwise stated, this configuration is to be considered. The number and configuration of the emitting areas can be varied, but the size of each emitter and average rate of photoemission for all of the emitters are the same. This is shown schematically in figure 4.1. The important parameters are: the gap spacing of the diode, D, the potential applied to the diode, V_g, the emitter radius, R, and the spacing between the center of adjacent emitters, L. It is assumed that electrons are ejected from the emitter, via photoemission, at a rate which is much greater than the space-charge limiting current. In other words, the current is never source-limited but always space-charge limited. It is assumed that the emission velocity is zero. This space-charge limit is inherently guaranteed by the algorithm used in the simulation as will be described subsequently.
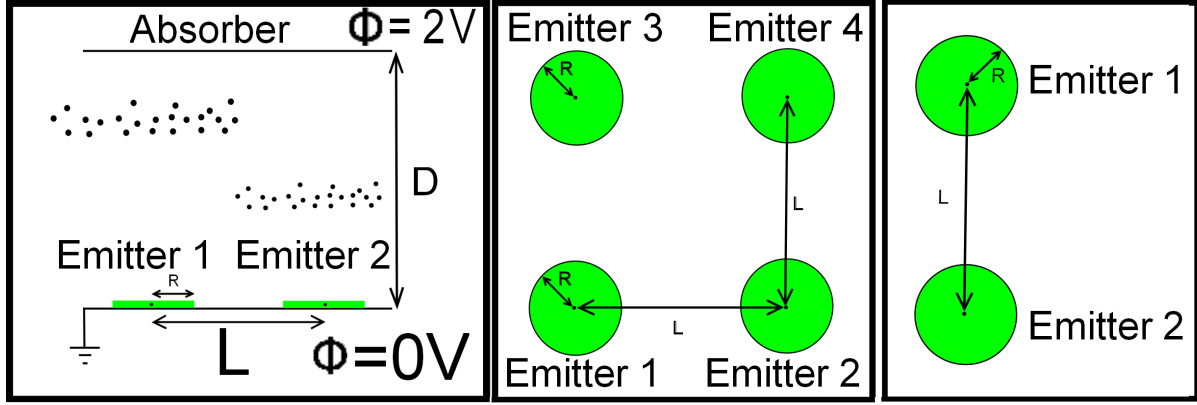
Figure 4.1: Side view of the microdiode showing a cross section taken through the center of two emitters with black dots representing electrons (left). Top view of the cathode showing a four emitter array (middle). Top view of the cathode showing a two emitter array (right).

4.2   Relative phase and the coupling parameter

The relative phase is a good indicator of how well the periodic pulses released by the two emitters are synchronized. In order to check the synchronization in our chaotic system we use the following method [57]: During the simulation we monitor the electrons released by each emitter. The total signal is just the sum of the two series of pulses produced by each emitter separately. We will denote the signal from the first emitter as $y_1(t)$ and the signal of the second emitter as $y_2(t)$. We will interpret the time variable t as an angular coordinate. By taking the Hilbert transform of the first signal we get $y_1(t + \tau)$. If the signal is purely harmonic, τ would just be the signal shift of $\pi/2$. $y_1(t)$ and $y_1(t+\tau)$ play the role of dynamic conjugated variables, and they produce the phase space limit cycle of the signal from the first emitter. From this limit cycle, the phase is easily extracted as $\phi_1(t) = \arctan\left[\frac{y_1(t)}{y_1(t+\tau)}\right]$. We do the same to the second signal, and from there we extract $\phi_2(t) = \arctan\left[\frac{y_2(t)}{y_2(t+\tau)}\right]$ [56].

ϕ_1 and ϕ_2 are the phases of the two chaotic oscillators due to the two emitters. If they are identical throughout time (or if the difference between them is a multiple of 2π), it would mean that the signals evolve in perfect synchronization. This is generally not the case however, but if the difference between them is close to being a multiple of 2π they are in near synchronization and add constructively. If the difference between the phases is an odd multiple of π, they are anti-synchronized and add destructively. If the phase difference moves freely without stopping either at a multiple of 2π or just an odd multiple of π they are merely unsynchronized. Examples of these three situations can be seen in fig 4.2 (bottom).

It is useful to have some sort of measure of the influence of the space-charge coming from one emitter on the surface field at the center of another emitter. We propose a coupling parameter to serve this purpose. Consider two circular emitters located on the cathode of the same planar diode, as shown in Fig. 4.1. The spacing between the centers of these emitters is L, the gap spacing is D, and the gap voltage is V_g. Let E_{nm} be the contribution to the electric field normal to the cathode at the center of emitter m, due to the space-charge that originates from emitter n. For example E_{21} is the contribution to the electric field normal to the cathode at the center of emitter 1, due to the space-charge that originates from emitter 2. The coupling parameter can then be defined as $C_{21} = E_{21}/E_{11}$ or $C_{12} = E_{12}/E_{22}$. In a symmetric system $C_{12} = C_{21}$. Although an exact measure of this parameter is problematic it can be readily estimated. If $\rho_1(x, y, z)$ is the charge density in the gap due to emitter 1,

and we consider the situation where emitter 2 is turned off, then a reasonable approximation is that the charge density inside the beam emanating from the emitter is solely a function of position above the cathode, z, and that $\rho_1(x, y, z) = \rho_1(z) = Kz^{-2/3}$, [32] where K is a constant. From symmetry we anticipate that the same applies to the charge density from emitter 2, when it is the only one emitting, i.e. $\rho_1(z) = \rho_2(z) = \rho(z)$. Assuming this form of charge density above either emitter, when they are both emitting, it is possible to estimate the position of the center of charge, z_c, above each emitter

$$z_c = \frac{\int_0^D z\rho(y)dz}{\int_0^D \rho(z)dz} = \frac{D}{4}. \tag{4.1}$$

If Q is the total amount of charge present in the gap due to one emitter, then one can estimate the coupling parameter, C, as

$$C \approx \frac{Qz_c/(z_c^2 + L^2)^{3/2}}{Q/z_c^2} = \frac{1}{(1 + 16\xi^2)^{3/2}}, \tag{4.2}$$

where $\xi = L/D$. Although this parameter is not exact, it serves a valuable purpose in giving a quantitative measure of the effect of the space-charge from one emitter compared to that from an adjacent emitter. Interestingly, it is solely a function of the ratio L/D.

The reader will note that the coupling parameter has a maximum value of $C = 1$ when $\xi = 0$, but drops off rather sharply. $C = 0.5$ for $\xi \approx 0.19$, while $C = 0.25$ for $\xi \approx 0.31$, $C = 0.1$ for $\xi \approx 0.48$, and C varies asymptotically with $1/\xi^3$. This suggests that, in space-charge limited flow, the surface electric field at a point is primarily affected by emission from an area within some normalized radius, r/D, around that point. This observation is supported by the structure of the two-dimensional Child-Langmuir law [32], [27], [58] where the normalized space-charge limited current density from an emitter of finite size scales as $1 + \frac{C_1}{S/D} + \frac{C_2}{(S/D)^2}$ where D is the diode gap spacing and S is the length scale of the emitter area, i.e. the dependence is on the normalized length S/D and two-dimensional effects are mostly important for smaller values of S/D.

4.3 Diode array analysis

We begin by examining a simple system of two emitters designed so as to keep the number of electrons in the gap larger than one, but as close to one as possible. This setting creates dynamics similar to the Coulomb blockade-a phenomenon known in the single-electron transport in quantum dots. To do this the radius of each emitter is set at 1 nm, the gap spacing is set at 18 nm, while the gap voltage, V_g, ranges from 0-300 mV, and the spacing between emitter centers, L, ranges from 0-90 nm (ξ ranges from 0-5). The next step is to systematically vary V_g and L, and record the phase difference between absorption, at the anode, of the k-th electron from the first emitter and absorption of the k-th electron from the second emitter.

Figure 4.2 shows results of this investigation. Referring to the top part of figure 4.2, the white area shows combinations of L and D where no synchronization takes place or the electrons are in anti-phase, the green color indicates a region where synchronization is persistent, and the red area a transition region where synchronization drops in and out. The colored regions are separated according to the mean of the phase difference μ and its standard deviation σ. Inside the green region both are small, i. e. $0 < \mu, \sigma < 0.1$. Transition
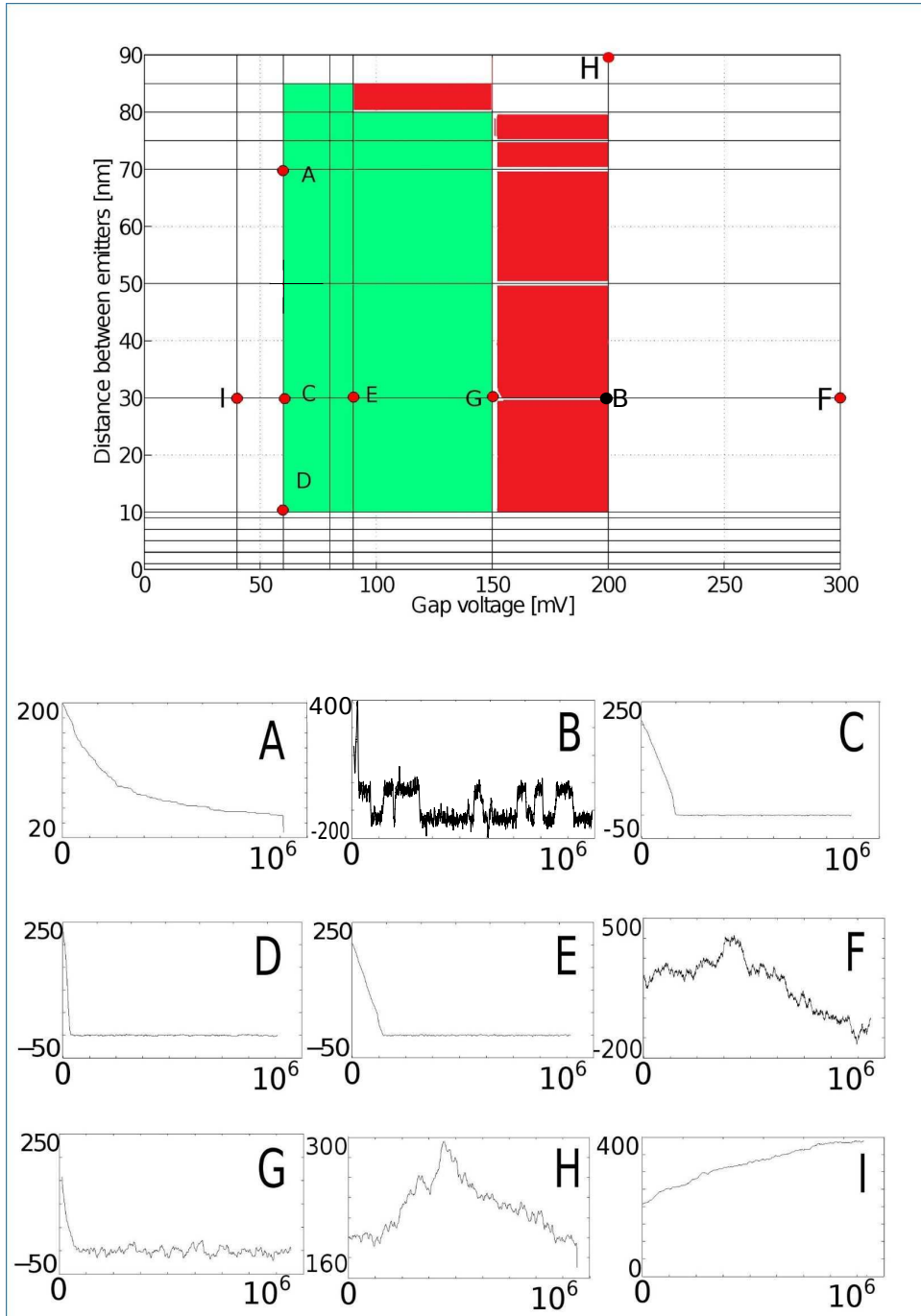
Figure 4.2: (Top) Synchronization region shaded green (or light grey in monochrome print), transition region in red (or dark grey in monochrome print) and the white region is the one where no synchronization is evident. (Bottom) The time delay diagram for each labeled point in the synchronization region and outside of it. The axes on each plot are: x-axis is the time given in time steps, y-axis is the delay given in number of emissions. In the beginning all diodes start with 200 time steps difference between each emitter.

happens where the mean is still small, $0 < \mu < 0.1$, but the standard deviation is large, i. e. $\sigma \gg 0.1$. This is also called near synchronization region. Nonsynchronous behavior is characterized by large values for both, i. e. $\mu, \sigma \gg 0.1$. The apparent sharpness of the boundaries is due to the limited number of points sampled. The bottom part of figure 4.2

shows examples of the development of the phase as a function of time for selected combinations of L and V_g. In these nine plots, the labels on the axes are the same: the x-axis shows the time given in time-steps from the beginning of the simulation and the y-axis depicts the interval between two successive arrivals from separate emitters. This means that the interval is zero if they arrive simultaneously. If they are synchronized, arrival will be either at the same time or at a multiple of the period, but this line should eventually become constant. If it is not constant, this is a sign of nonsynchronous signals.

The vertical boundary between the green and white region to the left of the green region is easily understood. This is simply an area where the applied voltage is too low to support more than one electron at a time in the gap, hence one cannot speak of synchronization. The horizontal boundary at $L = 10$ nm comes about because the close spacing of the emitters leads to electrons released from them alternately and thus arriving at the anode in anti-phase. The boundary at the top of the stable/transition regions is simply explained by the fact that the emitters are placed so far apart that their coupling is too weak to lead to synchronization. Loss of synchronization because of increasing gap voltage is not as clear cut, as evidenced by the transition region to the right of the green colored area in figure 4.2. The reason for this loss of synchronization is that at higher gap voltage, the number of electrons present in the gap increase, and due to the small emitter size this corresponds to a rather high charge density above the emitter. Thus mutual repulsion of the electrons disrupts the structure of the „beamlets" and leads to degradation of synchronization.

Next we examine systems where the emitter area, gap voltage and gap spacing are all considerably larger, whereby emission occurs in electron bunches rather than as individual electrons. This corresponds to the situation described in previous work [46], [49]. For subsequent simulations the gap spacing is fixed at $D = 500$ nm, the gap voltage at $V_g = 2$ V, and emitter radius at $R = 150$ nm. The time-step used in the simulations is 0.25 fs. All emitters are circular and flat.

When two emitters are synchronized, then their phases will change approximately together [57], thus the phase difference between them stay approximately constant, either as an even multiple of π for constructive synchronization, or an odd multiple of π for destructive synchronization. Transitions in phase difference between multiples of π, known as phase slips, may occur sporadically. In figure 4.3 the relative phase between current from a pair of emitters is shown for different values of the emitter spacing, L, ranging from 300nm, when the emitters are just touching, to 400 nm. For $L < 340$ nm the synchronization is persistent, and mostly without phase slippage. At $L = 340$ nm phase slippage occurs twice, and we note that during the time interval from roughly $2 - 4 \times 10^5$ time-steps (50-200 fs) the emitters are synchronized in anti-phase leading to destructive interference. For $L > 340$ nm the phase difference starts to fluctuate slowly, resulting in non-persistent synchronization.

The reader is now referred to figure 4.4. Closer examination, of the case where the two emitters are separated by $L = 400$ nm, is instructive. For the first 20 fs of the run, only one emitter is switched on. At that time emission from the other emitter is allowed to commence, and for the duration of the simulation both emitters are active.

In figure 4.4a the frequency spectrum for the entire signal can be seen. This includes a prominent peak at a frequency somewhat below 2 THz, and a small peak adjacent to it at a slightly higher frequency. The smaller peak is due to the portion of the signal when only one emitter was active for the first 20 fs. The drop in frequency is in accordance with theoretical considerations [46] and empirical evidence [49] that the bunching frequency should drop with increasing emitter area. Further discussion of this point will be made later.

In figure 4.4b a spectrogram for the same signal is shown. One may easily see the drop in frequency, and transient broadening of the spectrum, as the second emitter is turned on. Also
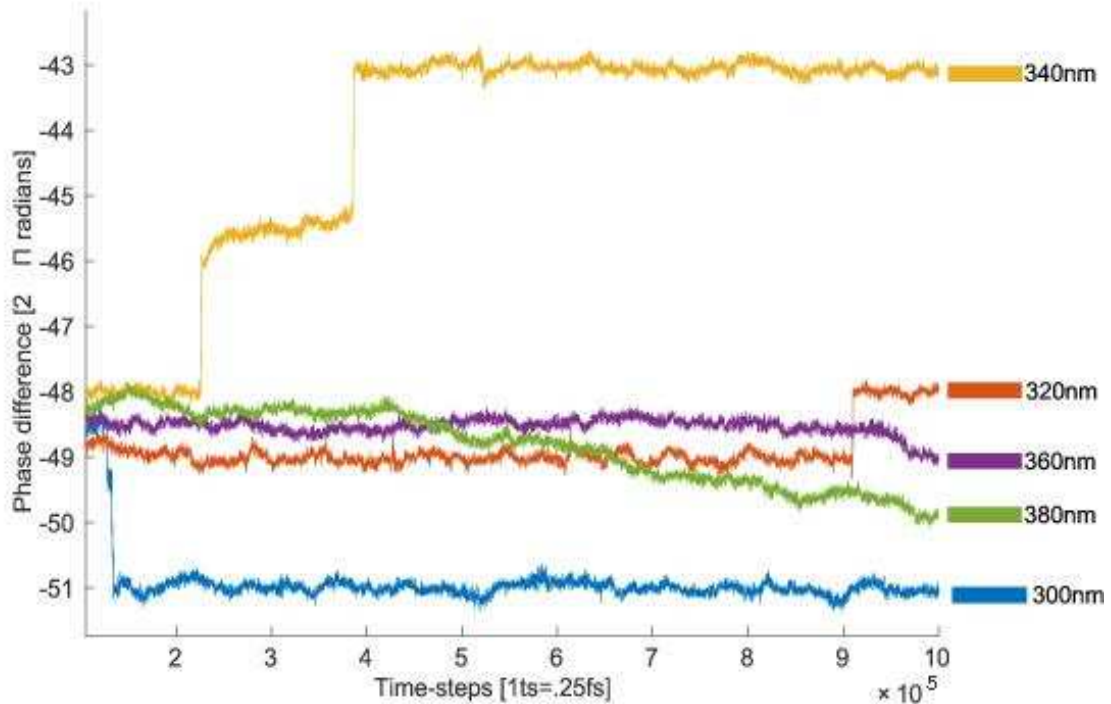
Figure 4.3: The phase difference between the signals from the two emitters. The numbers next to each curve show the distance between emitters' centers. There are clear "jumps" in the phase difference called phase slips which occur when the coupling between emitters becomes weak.

apparent is how the high frequency peak is eroded as the synchronization slips into anti-phase, or destructive interference, around 60-70ps and towards the end of the simulation. The erosion in the signal can be seen as decrease in the spectrogram during the mentioned time period. It can also be seen as a decrease in amplitude of the signal in the time domain in figure 4.4c and also as a phase difference close to the destructive π value in figure 4.4d.

In figure 4.4c the signal is shown in time domain. Apparent from this graph are the initial bursts of current as the emitters are turned on one after the other. These bursts happen because, initially, the electrons are being injected into an empty (or almost empty, in the case of the second emitter) diode gap with no space-charge to inhibit them. The strength of the synchronization shows up in the envelope of the signal oscillation and, by comparison with figure 4.4d, it is clear that the oscillation is strongest when the two emitters are in phase and weakest when they are in anti-phase.

We now turn our attention to the frequency of the total signal coming from multiple emitters. As previously stated, it is known that the frequency from a single circular emitter decreases with increasing emitter area, and we wish to see if the frequency of a signal from synchronized emitters will have a frequency higher than that of a single emitter of the same area. To test this we run a series of simulations where the frequency is measured as function of the normalized center to center spacing ξ. This is done for a 1×2 array and for a 2×2 array. The results are shown in figure 4.5.

It is seen that when the emitters overlap completely, the frequency is the same as that of a single emitter of radius $R = 150$ nm. For the 1×2 array it is clear that the frequency
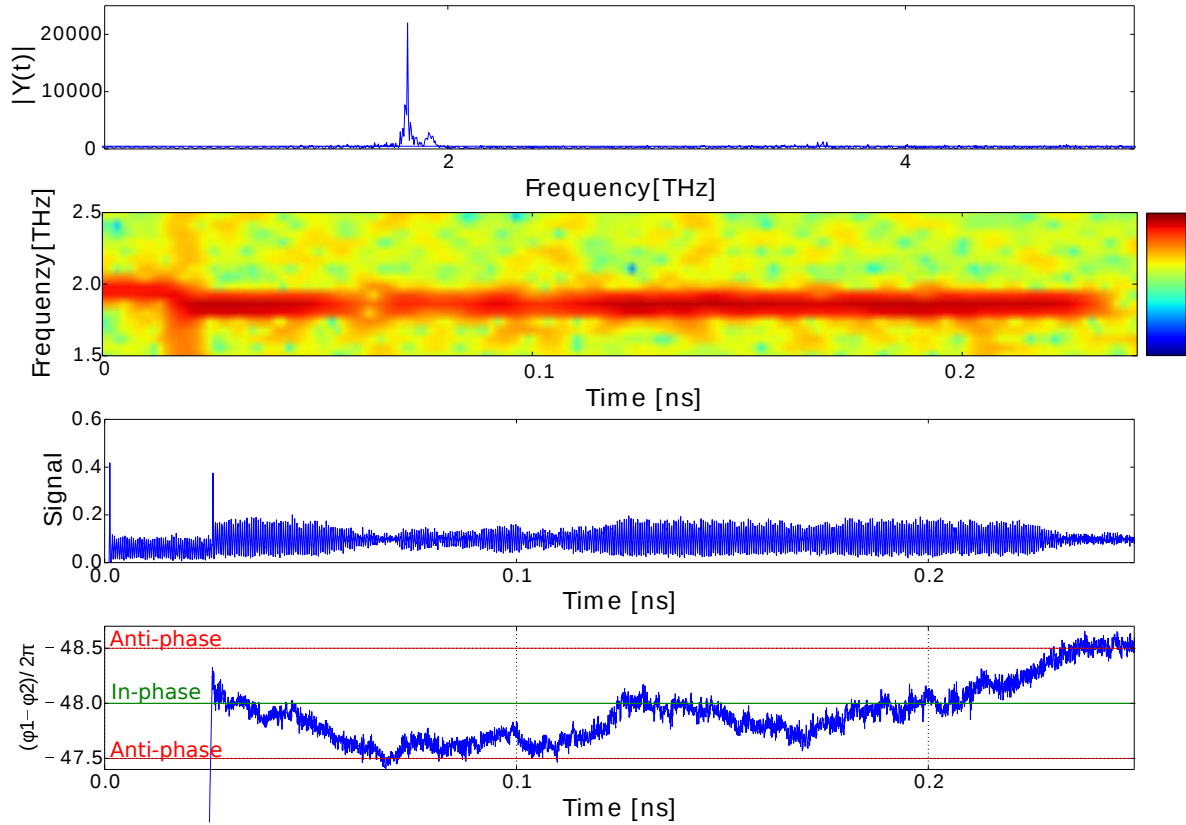
Figure 4.4: Compound picture showing (from top to bottom): a) the signal in frequency domain b) spectrogram of the signal c) signal in time domain, and d) relative phase (detailed explanation in text)

decreases over the interval $0 < \xi < 0.6$ due to the increased emission area. When $\xi = 0.6$ the emitters are barely touching, and as they are moved apart from each other they behave increasingly like independent emitters. Thus, the frequency is at the minimum with the emitters just touching, the frequency grows as they are pulled apart. The reader should note that the frequency of the signal from two separate emitters is always greater than the frequency from a single emitter of the same area. A similar result can be seen for the 2×2 emitter array. The minimum frequency is obtained as the four emitters are barely touching, and the frequency from four separate emitters is always higher than that from on single emitter of the same area. Additionally, it should be noted that the disparity in the frequency between four emitters and a single emitter of the same area, is greater than the corresponding disparity for the 1×2 array. This may indicate better coupling in the larger array. It should also be noted that the frequency is very consistent over multiple runs using fixed parameters, hence error bars have been omitted.

A similar investigation is done for the power of the THz signal. For each parameter combination 10 runs of the code are performed and the power is calculated. Figure 6 shows the normalized power of the signal from a 1×2 array as a function of the normalized separation. The power of the signal from completely overlapping emitters is one fourth of the maximum power (when the two emitters are barely touching). It can also be seen that power increases monotonically with increasing emitter area (i.e. in the interval $0 < \xi < 0.6$). As the emitters are pulled apart two items of interest can be observed. First, the total power decreases. Second, the variance in measured power output, from the 10 different runs for
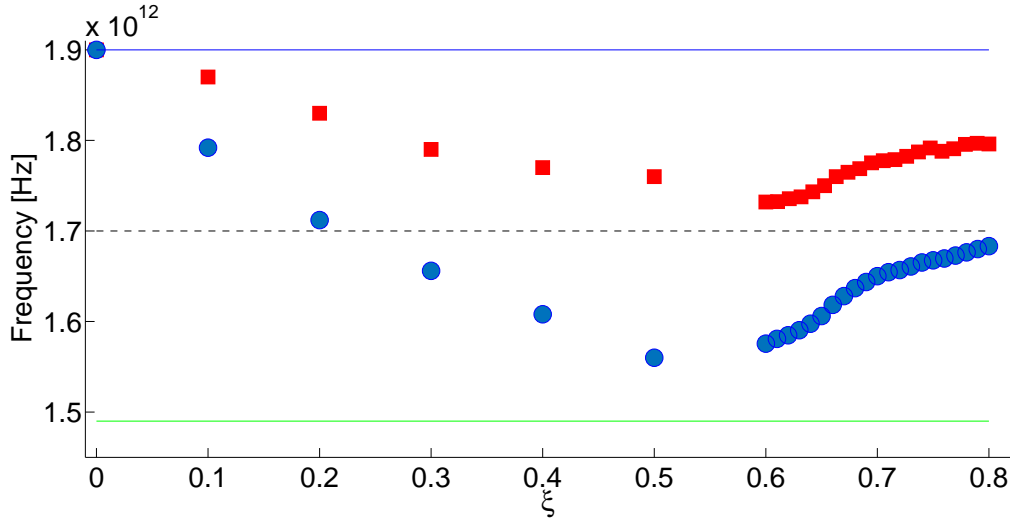
Figure 4.5: Frequency dependence on the normalized center to center distance ξ. The gap voltage is V_g = 2V, gap spacing is D = 500 nm, and emitter radius is R = 150 nm. For $\xi < 0.6$ the emitters overlap and for $\xi = 0$ one emitter is completely superimposed upon the other. Blue circles show the frequency of the signal from the 2×2 array, the top solid line indicates the frequency from a single emitter of radius R = 150 nm. The middle dotted line is the frequency from a single emitter of radius R = 212 nm. The red circles show the frequency from a 1×2 array and the bottom solid line shows the frequency from a single emitter of radius R = 300 nm.

each parameter set, increases. This means that the coherence of the signal diminishes quite rapidly with separation beyond touching.

Let us now consider N sinusoidal signals of equal magnitude and phase, but varying frequency: $i_k = \sin(\omega_t + f_k)$ for $k = 1$ to N. These signals are added together to form a compound signal $i_s = \sum_{k=1}^{N} i_k$. If we let P denote the time-averaged power of signal i_k (for $k = 1, 2, ..., N$) and P_s denote the time-averaged power of the compound signal, then one can readily see that

$$P_s = \frac{\omega}{2\pi} \int_0^{2\pi/\omega} i_s^2 dt = NP + 2P \sum_{r \neq s} \cos(\phi_r - \phi_s), \tag{4.3}$$

where the sum is taken over all $(N^2 - N)/2$ possible combinations of $r \neq s$ with r and s taking integer values from 1 to N. The highest achievable value for P_s, if all signals are in phase, is $N^2 P$ and the power averaged over a uniform distribution of oscillator phases, f_k, is NP. For the special case of $N = 2$, we see that P_s can range from 0 to $4P$ with a value of $2P$ when averaged over phase difference between the signals. From figure 4.6 it can be seen that the average power from two separate emitters tends to cluster around twice the power from a single emitter, and that the variance also increases as the separation grows. Additionally a signal, $g(t)$, from one emitter is generated a time shifted signal, $g(t - \tau)$, produced from it. From this, a compound signal $G(t; \tau) = g(t) + g(t - \tau)$ is constructed. Hence, the power carried by $G(t; \tau)$ can be calculated and averaged over τ. This average power is shown open circles in figure 4.6, and matches the expected value of twice the power from one emitter quite well.
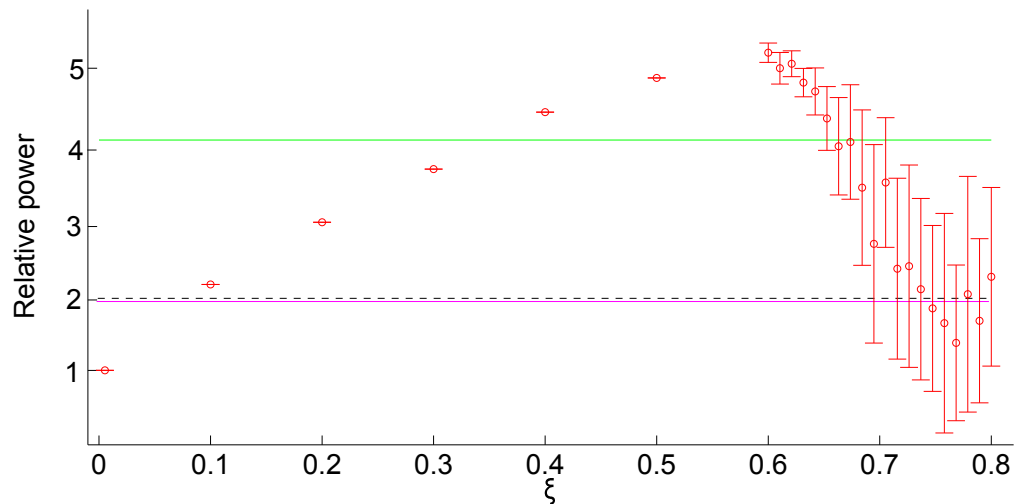
Figure 4.6: (Two emitters) After performing the Fourier transform of the total signal, we take a region centered around the main frequency peak and take the integral under the curve. This gives us the power of the signal in this region. The power of the signal in this region is actually the power that we would be extracting from the device. As the emitters are pulled further apart the power of the total signal drops. The green full line represents the power of one emitter. The black dashed shows twice the power of one emitter and this is coincidentally the same as the average power of two uncorrelated signals (full pink).
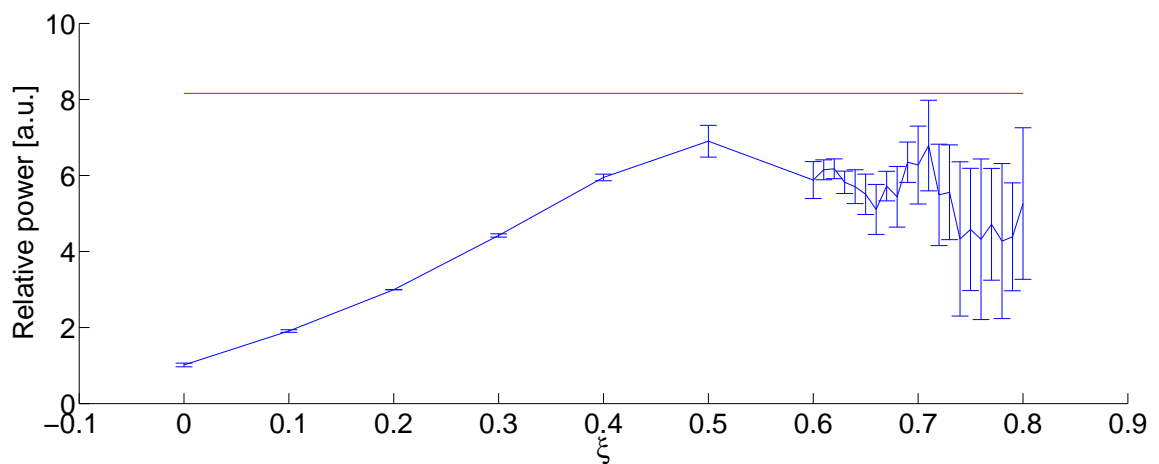
Figure 4.7: (Four emitters) Power of 2×2 array. The red full line represents the power of one emitter with identical area as four single emitters of R=150 nm.

Also shown in figure 4.6 is the power from a single emitter of the same area as the two separate emitters. One may observe that this power is slightly less than the peak power obtained with two emitters barely touching.

The results shown in figures 4.5 and 4.6 also show the the short range effects of coupling. At $\xi = 0.6$ the emitting disks are touching and synchronized. For $\xi = 0.8$ the normalized distance between the disk edges is 0.2 and synchronization between them has been lost.

Figure 4.7 shows how the power is affected by the emitter separation, ξ, in a 2×2 array of emitters. Each emitter has a radius of 150nm. It is apparent that the 2×2 array shares similar characteristics with the 1×2 array with the relative power increasing as the overlap decreases. However, in this case the peak power occurs at $\xi = 0.5$ rather than $\xi = 0.6$ as before, and does not match the power output of a circular emitter of 300nm radius. As in figure 4.6 we can see that for $x > 0.7$ phase synchronization seems to vanish as the power distribution is more similar to what would be expected from four independent emitters.

4.4   Summary of results obtained for emitter arrays

Previously we have shown that, under certain conditions, space-charge limited current from an emitter of limited area in a planar microdiode, will spontaneously form bunches so that the beam current is modulated with a frequency in the THz regime. The frequency is dependent on the applied field with which it grows according to a power law, and also upon the size of the emitter, with the frequency decreasing as the emitter area increases [49]. We have now shown that the current from individual emitters can synchronize via Coulomb interaction, if the emitters are not too far apart.

For a given applied field and total emitter area, the frequency of the synchronized system depends on the spacing between the emitters, but is greater than the frequency from a single emitter in all cases. The power coming from two circular emitters, that are barely touching, is shown to slightly exceed the power from a single emitter of the same total area. However, the average power from the emitter pair drops off rapidly as the distance between them is increased, settling around a value that corresponds to the average power from the sum of two sinusoidal currents with the same frequency but randomized phase difference. This indicates that frequency locking is much more persistent than phase locking.

Similar results are observed for the 2×2 array, although the gain in power is not the same as for the 1×2 array. On the other hand the 2×2 array shows better frequency characteristics than the 1×2 array in the sense that it is proportionally higher than the frequency from a circular emitter of the same area as the array.

We also show that for a simple system consisting of electrons coming from two point emitters a certain parameter range, in terms of applied field and spacing between emitters, leads to synchronization. In other words, a „sweet-spot" for synchronization exists.

The reader should note that in these simulations the we make the assumption of zero initial velocity of the electrons. This is a significant approximation when compared to the gap voltage of the diode, which is of the order 1 V. Rudimentary investigations show that a spread in initial emission energy corresponding to 1% of the energy at the anode is allowable for formation of space-charge induced bunches [49].

Our simulations show that it is possible to extract more power, at a higher frequency, from an array of emitters than would be possible from a single emitter of the same total area. To examine how this effect may be optimized, and how it applies to large arrays, is beyond the scope of this work but should be examined in future work both via simulation and experiment. Examination of stronger coupling mechanisms than the simple Coulomb interaction also merit further investigation.

We can see from several angles that producing THz radiation with the proposed devices is viable. Such a device would be tunable within a certain range depending on the radius of the emitters. Synchronization of several of such emitters is possible to achieve coherent radiation as a sum of all, but the inherent stochastic character of the emitters adds a fair amount of noise and thus making such a system limited to less than ~ 10 emitters. Although

this cannot increase the output power significantly, it can still bring it into the mW region, which might be useful for research applications or just as proof-of-concept. This device would have all emitters synchronize with each other and none would be more important than any other.

Another idea for future work might be having such emitters synchronize through the following procedure. One emitter works independently and the created small voltage V_{master} is fed into the gap voltage V_G. This would create a small oscillation on top of the comparatively very large V_G. This altered gap voltage is then fed into an array of emitters similar to the one before, except for the fact that they are separated from one another enough ($\xi >> 1$). This would render them independent emitters. Such emitters would not be able to create coherent radiation if it weren't for the small kick supplied by the V_{master}. Due to it, even noisy oscillators might be able to synchronize, of course within certain parameters. Such a setup should be a part of future investigation.

Chapter 5

Thermal Effects

5.1 Introduction

Although THz generation and applications [1], [4], [6], [8] are an interesting idea , there is still a fundamental issue that needs to be addressed. Under what circumstances can one expect to still see the time dependent structure intact? Two particular candidate causes for degradation of the beamlets are: velocity spread (or emittance); and Coulomb forces causing beamlets to expand and merge. We will now investigate the issue by looking in detail at how diode gap spacing, applied potential and velocity spread of electrons emitted from the cathode influence pulse formation and degradation.

5.2 Physical and simulation setup

The system under study is the infinite parallel plate vacuum diode, with gap spacing D, sketched in Fig. 5.1. Emission from the cathode is restricted to a circular area of radius R = 150 nm. The voltage applied across the diode is the gap voltage, V_g, and it is kept constant throughout one simulation. The vacuum field for a diode without any electrons in the gap is E_g.

Our previous work [49] explores the THz oscillations in depth for an initial electron velocity $v_{0e} = 0$. In this chapter we consider non-zero initial velocities.

For the photoemission process [59], [60] we will divide the emission region into two separate regions: metal and vacuum. The energy of electrons inside the metal corresponds to the free electron gas and it is governed by the Fermi-Dirac statistics. The energy of the vacuum state is $E_F + \phi_{eff}$, where E_F is the Fermi energy and

$$\phi_{\mathrm{eff}} = \phi_{\mathrm{w}} - \phi_{\mathrm{S}} = \phi_{\mathrm{w}} - e\sqrt{\frac{eE_g}{4\pi\epsilon_0}} \ . \tag{5.1}$$

ϕ_{w} is the work function and ϕ_{S} is the Schottky work function and this is the height of the photoemission potential barrier. The energy after emission is equal to $E + \hbar\omega - \phi_{eff}$. If the laser used for photoemission can be tuned such that $\hbar\omega = \phi_{\mathrm{w}}$, then the electron energy will be distributed by the Maxwell-Boltzmann statistics [61]–[65]. The Fermi-Dirac distribution is virtually identical to the Maxwell-Boltzmann distribution for energies higher than $1.005E_F$ at room temperature and this justifies using Maxwell-Boltzmann for the electron density of states [63]. Also, the electrons available for emission come only from the highest energy states. Our aim now is to try to model room temperature device, therefore the interest is in the high temperature tail of the distributions.
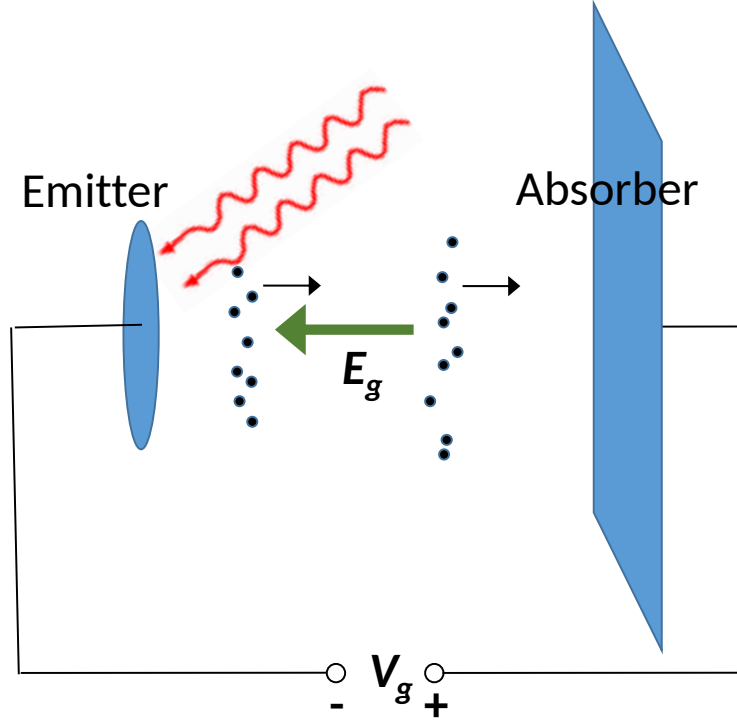
Figure 5.1: The device is a vacuum diode with a disk-shaped emitter on an infinite cathode under a strong laser pulse. The electrons are extracted in bunches and are driven to the absorber (anode) by the electric field E.

We consider the Maxwell-Boltzmann distribution of electron velocities at the emitter surface, in the spatial direction $i = \{x, y, z\}$,

$$f_v(v_i) = \sqrt{\frac{m}{2\pi k_{\mathrm{B}}T}} \exp\left(\frac{-mv_i^2}{2k_B T}\right) , \tag{5.2}$$

m being the mass of the electron, k_B, the Boltzmann constant, and T, the temperature. The velocities in the propagation direction, z, i. e. from left to right in Fig. 5.1, can only have positive values, whereas those in the perpendicular directions x and y can take any numerical value.

5.3 Results and analysis

We will now show the results in parameter space. The temperatures tested are $T = 0$, 1, 2, 4, 8, 16, 32, 64, 128, 256, 300 K. They are shown on the horizontal axes in the following figures. The gap spacing, i.e. the distance between emitter and absorber, has values $D = 50, 100, 200, 400$ nm, shown on the vertical axes. Each figure is made with a fixed value of the electric field, $E_g = 1, 2, 4, 8, 16, 32, 64, 128$ MV/m.

For each combination of parameters we run six simulations. Each simulation is run for 2.5×10^5 time-steps which brings the total simulated time to $t_{tot} = 6.25 \times 10^{-11}$ s. For the systems with lowest frequencies ($f_{min} \approx 0.8$ THz) we get ~ 50 bunching events and for the highest frequencies ($f_{max} \approx 2.2$ THz) about 140 bunching events in total. We begin the presentation with the averaged signal-to-noise ratio (SNR).
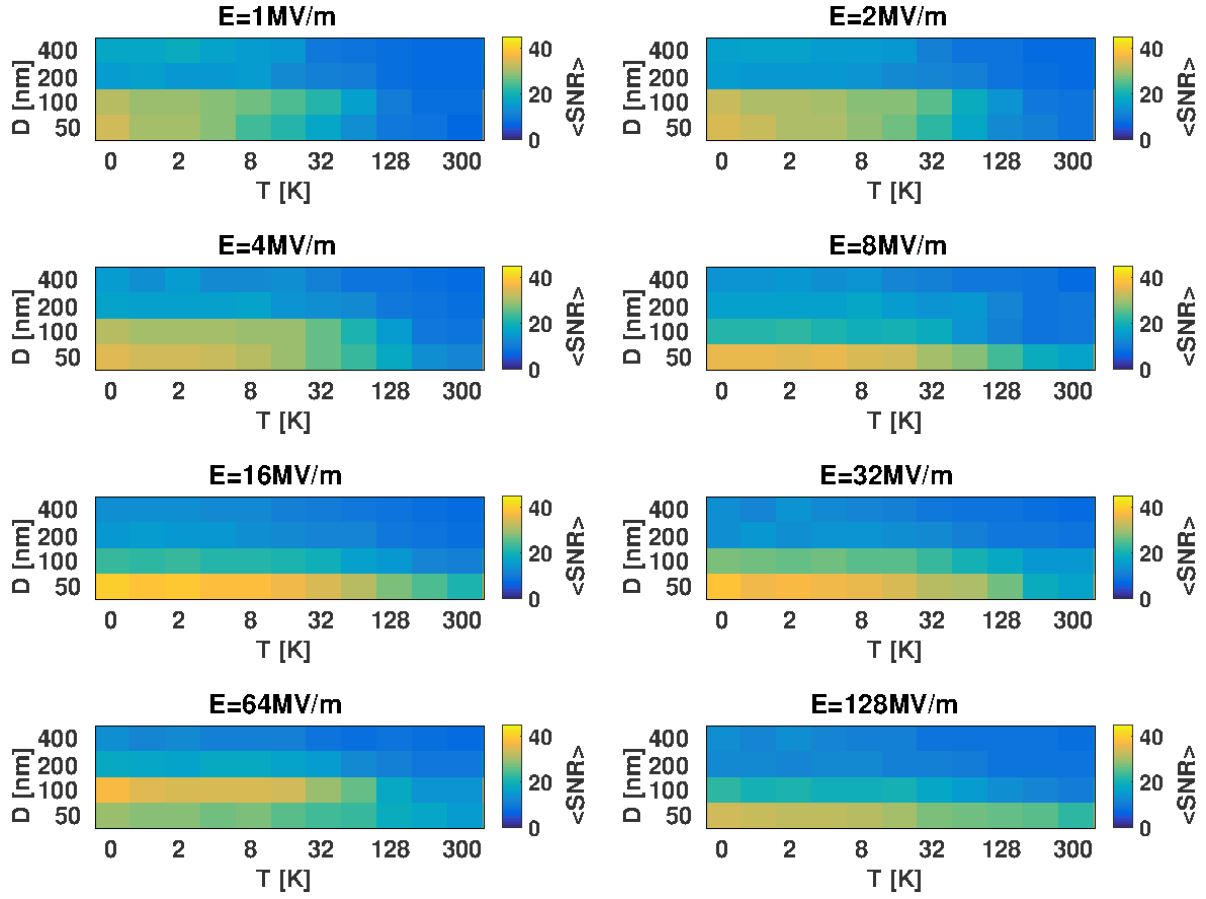
Figure 5.2: The averaged signal-to-noise ratio, $< \mathrm{S}NR >$.

5.4 Averaged signal-to-noise ratio, $< SNR >$

The results clearly show that a strong THz signal is carried by the current even if the initial velocities correspond to room temperature. This is true only if the electric field is strong enough. The algorithm for the calculation of the SNR uses unfiltered Fourier transform and searches for the highest peak in a predetermined region. This region can be found through

$$f = A \times E_g^\alpha \tag{5.3}$$

given in [49] where f is the frequency measured in Hz, and E_g is the applied vacuum field measured in V/m. The parameters A and α depend on the size of the emitter, i.e. the radius of the disk. Table 5.1 shows the values of the parameters A and α for three inspected emitter radii.

If the spectrum contains higher harmonics, as it often does, the algorithm chooses only the first harmonic for the analysis. Although higher harmonics can carry a significant portion of the energy, keeping with the conservative nature of this research, only the first, and always highest, peak is chosen.

The noise level is measured as an average noise away from the peaks. If the height of the signal peak is A_s, and the average height of the noise is: A_n, then the signal-to-noise ratio in decibel is SNR [dB] $= 20 \log_{10}(A_s/A_n)$. From the plot for the average SNR in Fig. 5.2, we can notice: For low vacuum fields, $E_g < 8$ MV/m, at low temperatures, $T < 256$ K, it is evident that the signal quality is governed by the temperature, but not so much by the gap spacing, since we can see that there is a spread of higher quality signals even for larger gaps of $D = 100 - 200$ nm. As the vacuum field increases above $E_g = 8$MV/m the higher signal

Table 5.1: Magnitude of the parameters in Eq.5.3, $f = A \times E^{\alpha}$, for different values of the radius of the emitting area

Emitter radius [nm]	A	α
50	779×10^6	0.539
100	326×10^6	0.580
250	257×10^6	0.575

quality concentrates at the low gap spacing region, $D < 200$ nm. This is due to the fact that as the vacuum field increases, so does the number of electrons per bunch. This creates ever increasing intra-bunch forces due to the electron-electron repulsion and thus bunches are destroyed before they can reach the anode.

5.5   Average number of electrons per bunch, $< EPB >$

Next we show the results for the average number of electrons per bunch $< EPB >$ and the average number of bunches in the gap, $< BIG >$. Interestingly, the BIG shows that signal quality decreases with and increasing number of bunches in the gap. This basically means that the THz signal is the strongest when BIG ≈ 1.
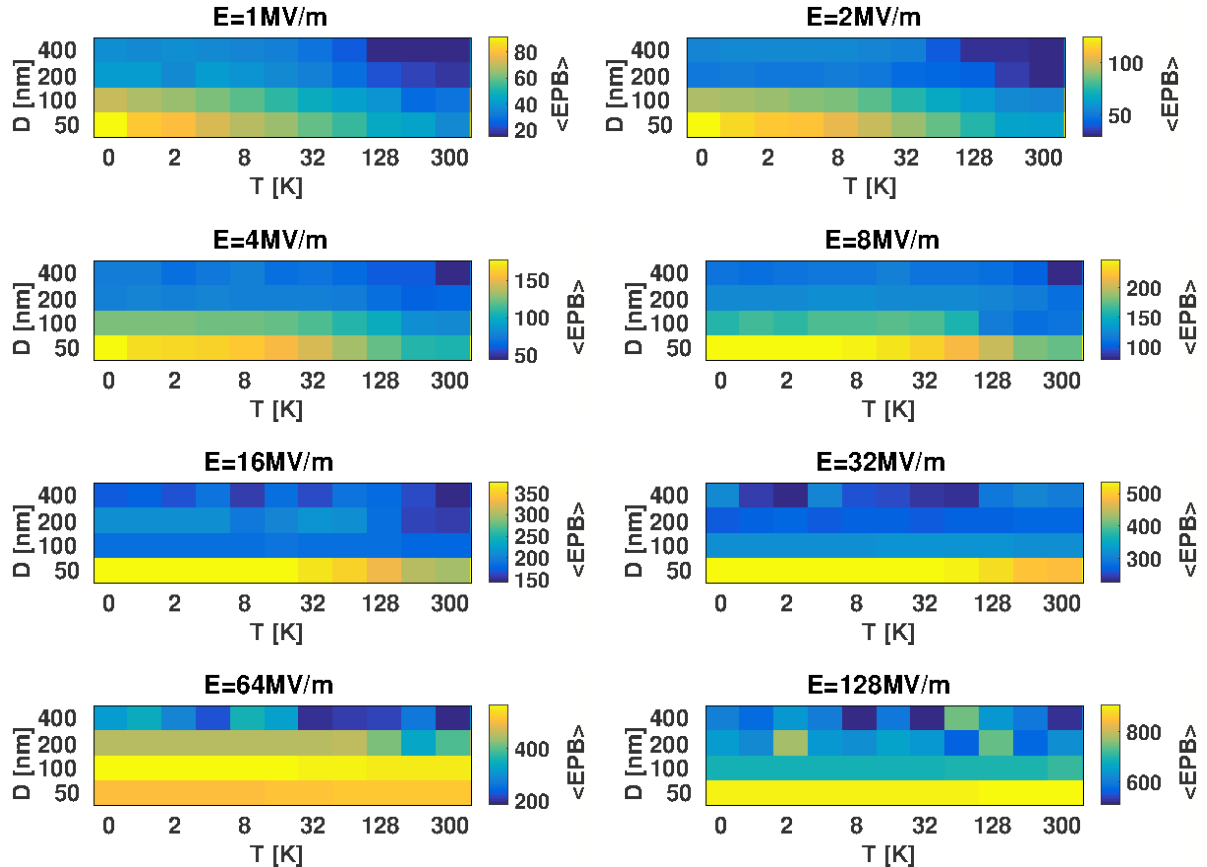

Figure 5.3: Average number of electrons per bunch, $< EPB >$.

The number of electrons per bunch increases with increasing electric field due to the fact that more electrons per bunch are needed to create field reversal at the emitter surface [46]. It also increases with decreasing the temperature, since the bunches have more definitive structure and less smearing, Fig. 5.3. This creates robust and solid bunches which block the cathode for a long time before another bunch is formed. As the temperature is increased, bunch destruction begins much faster after formation. Because no real blockade on the cathode is created, another bunch forms much sooner than it would happen at a lower temperature. This might mean more bunches in the gap with increasing temperatures, as can be seen in Fig. 5.4, but these bunches each have fewer electrons, and the current begins to resemble a continuous stream.
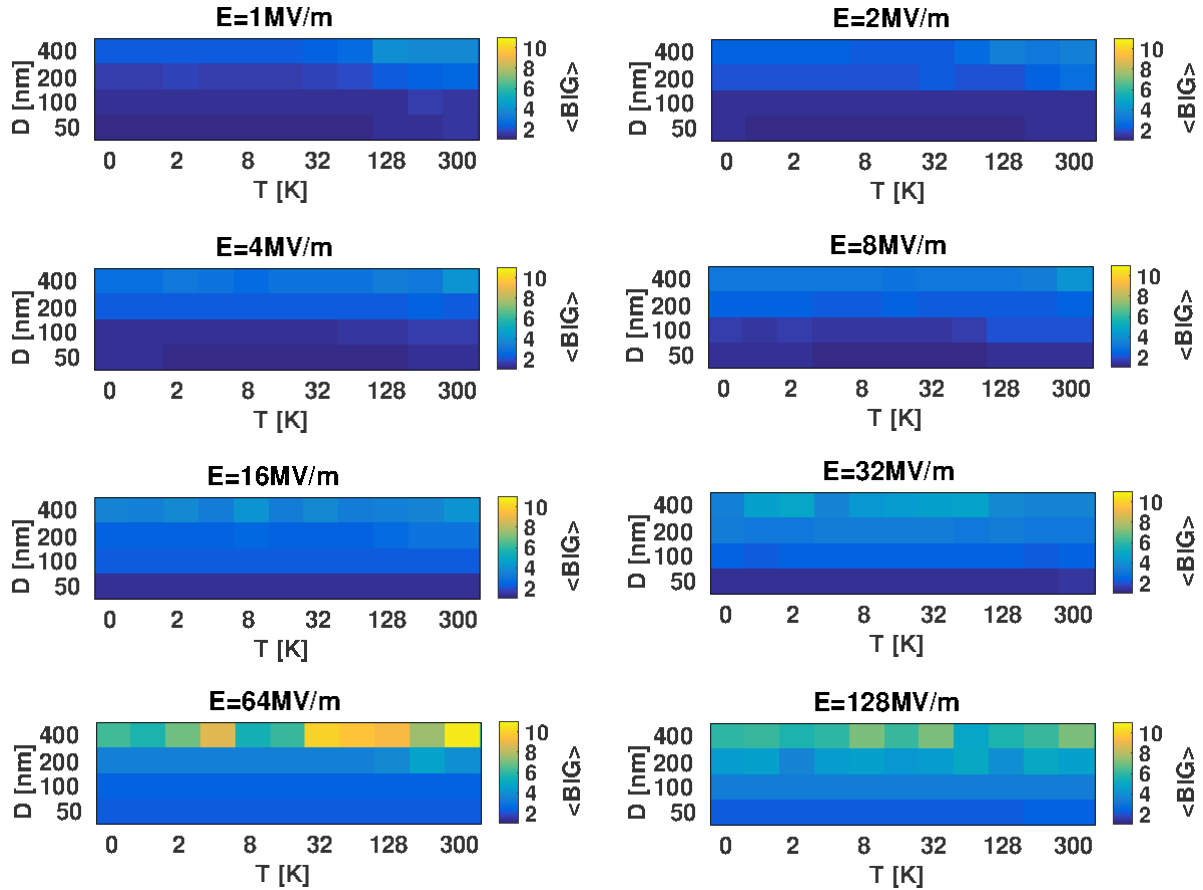
Figure 5.4: Average number of bunches in the gap, $< BIG >$.

5.6 Average number of bunches in the gap, $< BIG >$

The number of bunches in the gap increases with increasing vacuum field, gap spacing, and more subtly with temperature. As the vacuum field increases, the total number of electrons in the gap also grows and this means more bunches in the gap. This comes from the simple Child-Langmuir law [66]. Similarly, increasing gap spacing means more space and more bunches can be accommodated into it. As the temperature increases, the initial velocity of the electrons increases as well. This lowers the blocking potential from the charge already present in the gap, the emission is facilitated, and the virtual cathode from the electrons already present in the gap can be more easily overcome. If the temperature is low, all elec-

trons exit the emitter with similar velocities and the bunch is more narrow in the direction of propagation.

Figure 5.5: Average peak frequency, $< f > [\text{H}z]$

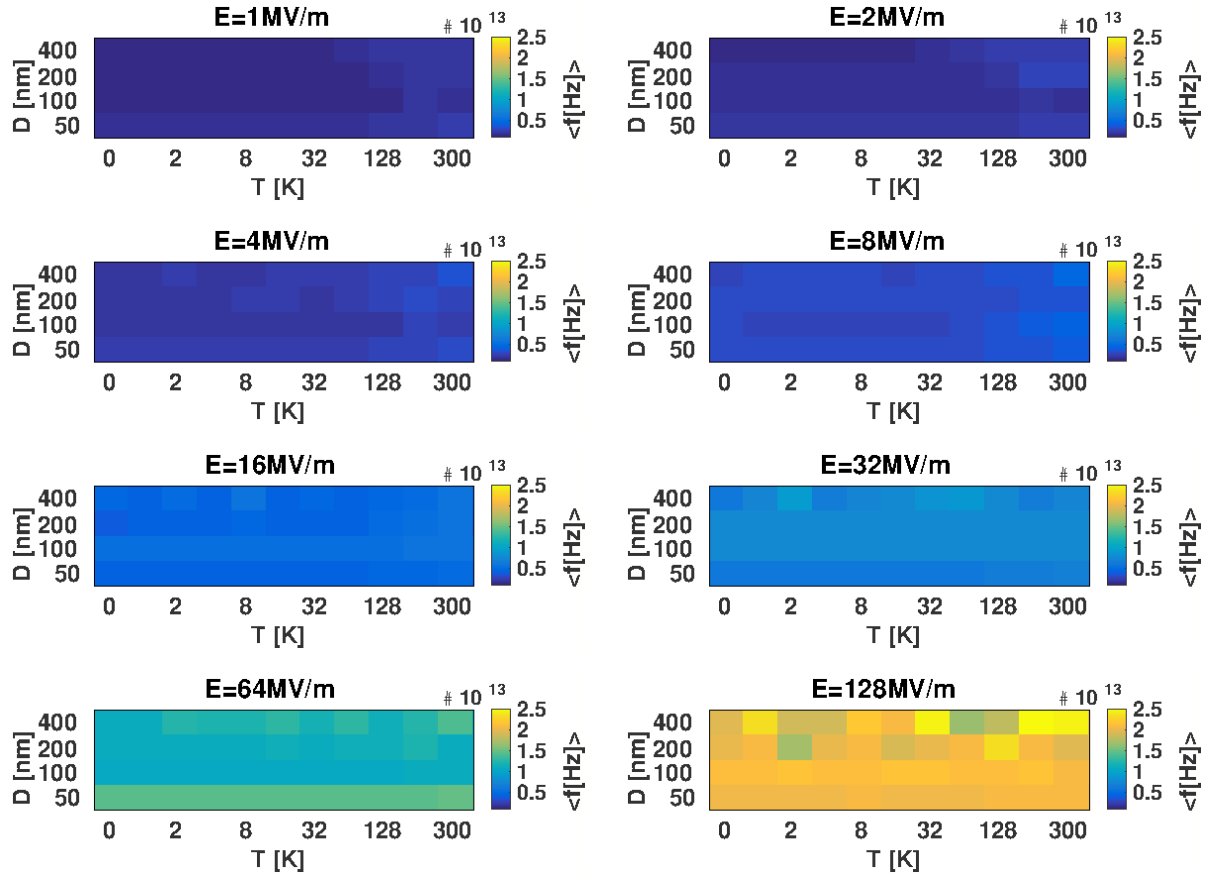## 5.7   Bunching frequency

It has been shown [49] that the current frequency depends only on the electric field for zero emission velocity. That is why all the plots of Fig. 5.5 show roughly homogeneous color; the frequency doesn't change with changing temperature, nor gap spacing. As the temperature increases, bunches begin to increase in size and to merge, and the SNR decreases. The first harmonic in the Fourier spectrum, which is used to determine the frequency widens and that is why there can be seen wider variations in color once the temperature and gap spacing are very high.

The average number of electrons in the cathode-anode gap in Fig. 5.6 for every vacuum field is obtained by taking the average of all of EIG for all temperatures and gap spacings for the particular electric field. This number increases simply due to the increasing space-charge limited current density given by the classical Child-Langmuir law [66]. On the same figure we can see the average number of electrons per bunch, $< EPB >$. This was done as a way to cross check our work with previous work [48].

5.8 Conclusion regarding the effects of temperature

THz radiation with microdiodes where several bunches are present in the gap can be maintained only at low temperatures $T < 10K$. Although such temperatures are attainable, they are impractical for real world operation. In this chapter we showed that if the number of bunches in the system can be controlled to be close to one, the SNR significantly improves. Such systems can have a signal with high SNR (> 25 dB) even at room temperature.
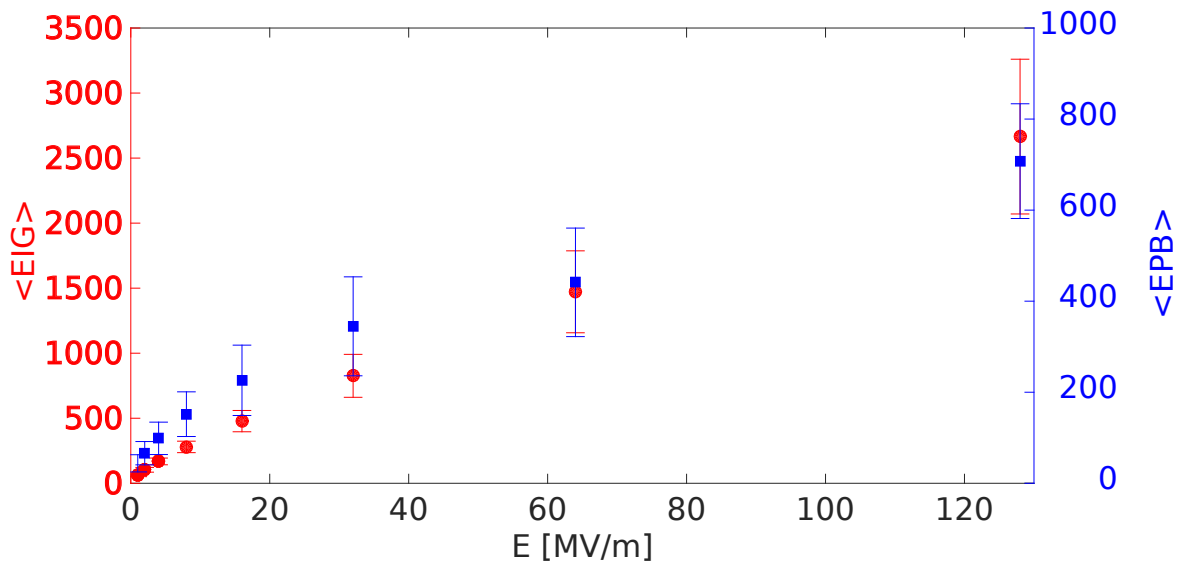

Figure 5.6: Average number of electrons in the cathode-anode gap, $< EIG >$ (red circles) and average number of electrons per bunch, $< EPB >$ (blue squares).

Chapter 6

Space Charge Effects in Solar Cells

During the research done on this PhD program one question arose with time. Namely, what would be the consequences of the space-charge effects in a semiconductor material? For example, in a solar cell. The in-house code was adapted for this purpose and it was tested in various scenarios. In the following sections we describe the dynamic I-V characteristics of a diode made of a semiconductor material in the presence of a photon flux which generates electron-hole pairs. We obtain hysteretic I-V loops which are related to the space-charge dynamics. The transient charge response determines a phase shift between a time periodic applied voltage and the corresponding current passing through the diode. Two such scenarios are presented in the following sections. The case of the silicon material, which is the most commonly used for solar cells, and the case of a hybrid organic-inorganic material, i. e. methylammonium - lead - halide ($CH_3NH_3PbI_3$), which contains molecular dipoles.

6.1   Solar cell simulation - silicon case

This series of simulations is done on a silicon based solar cell. The main material parameters are the effective masses of electrons and holes (m_e^* and m_h^*), their mobilities (μ_e and μ_h), and the band gap (E_g). Other details like the crystal structure, defects, or impurities, are included in these effective parameters. For the purpose of simulating the solar spectrum we used Reference Solar Spectral Irradiance ASTM G173 shown in fig.6.1.

The solar cell consists of a rectangular parallelepiped (cuboid), Fig. 6.2, on which two opposing sides separated by distance d are submitted to potential difference, V_c. From the ASTM G173 solar spectrum the probability of incidence of photon is calculated. This photon has energy E_{ph}. The band gap energy for silicon is $E_g(\text{Si}) = 1.11$ eV, and room temperature $T = 302$ K is assumed [68]. The photon strikes a random point inside the cuboid. If the energy of the photon is smaller than the band gap energy, $E_{ph} < E_g$, the photon just passes through. Otherwise an electron-hole pair is created. The rest of the energy $\Delta E = E_{ph} - E_{bg}$ is proportionally divided among the electron and the hole. This gives them an initial velocity v_{oe} for the electron and v_{oh} for the hole. These velocities are pointed in random directions and have uniformly distributed velocities. Although this picture might not be entirely true and additional photon-electron scattering effects could be included, for the first version of the software the present approximations were considered sufficient.

As both charge carriers move, the photo-generated current i is calculated as

$$i = \frac{1}{d} \left(\sum_{holes} ev_{oh} + \sum_{electrons} -ev_{oe} \right) , \tag{6.1}$$
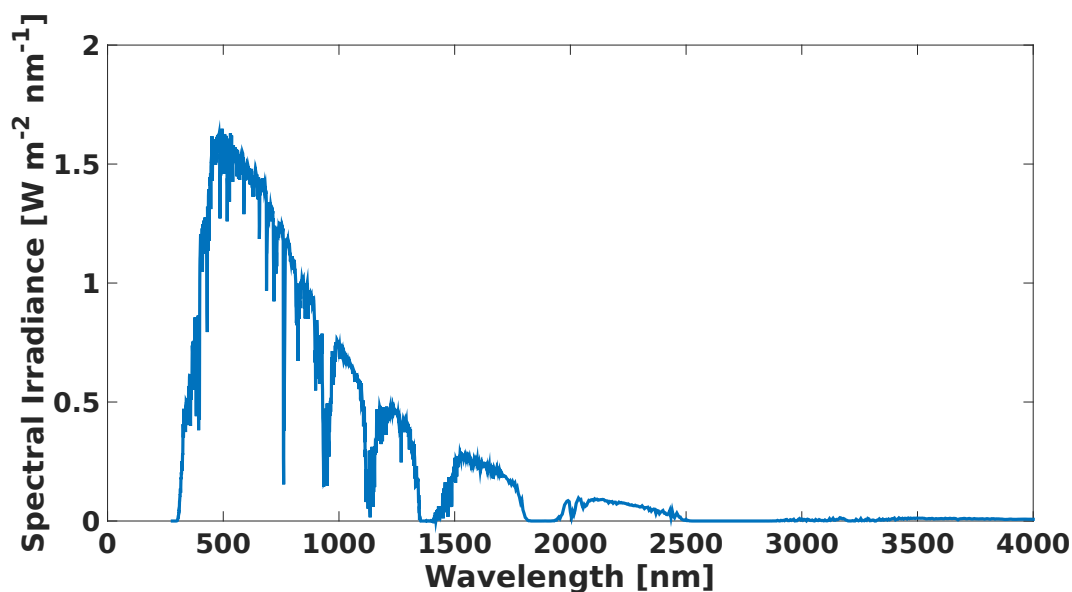
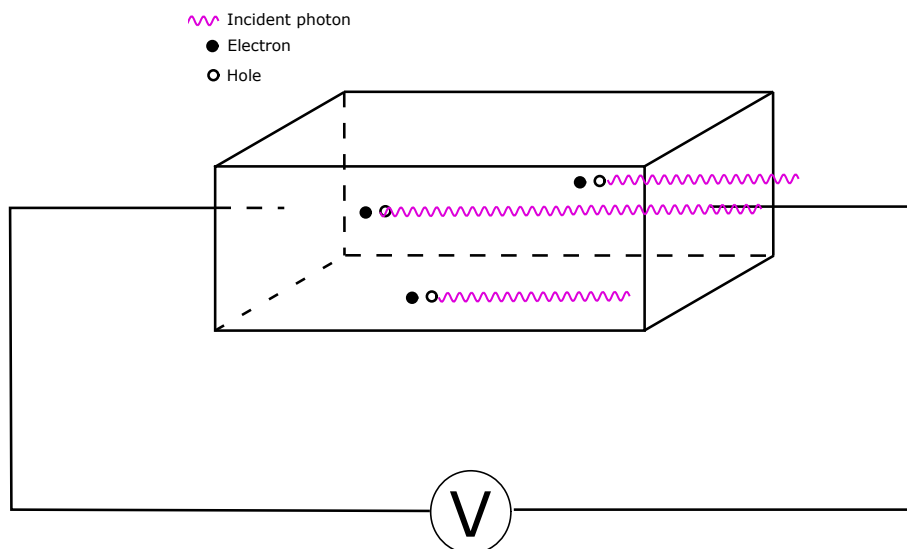Figure 6.1: Reference Solar Spectral Irradiance ASTM G173 as given in [67]

Figure 6.2: 3D structure of the solar cell simulation system. The photons are incident from right to left, through the lateral surface, which is supposed to be a transparent electrode.

where it is assumed that the incident photons enter into the diode through the lateral surface of the device as shown in Fig. 6.2. This is the Ramo-Shockley current [69], [70]. Once an electron or a hole passes any of the sides of the cuboid it is absorbed and removed from the simulation. Forces are calculated between each and every one of the charge carriers (electrons and holes) according to the molecular dynamics method, as before. While in the previous simulations the medium was vacuum, now it is a silicon lattice. In principle the motion of the charge carriers is now restricted due to collisions with the Si lattice in thermal vibrations or with impurities. In order to incorporate the collisions, instead of finding the net vector of the force on each particle and then calculating the acceleration like before, the velocity Verlet method has friction term included. That reduces the steady-state velocity to the drift velocity $v_d = \mu E_{sc}$ where $E_{sc} = V_c/d$ through the mobilities for electrons, μ_e, and holes, μ_h, separately. In other words, the collisions are treated like friction. In addition to these forces, the Coulomb forces between carriers create acceleration.

The de Broglie wavelength is $\lambda = h/p$, h being the Planck constant and p, the particle's momentum. The root mean square speed from the Maxwell-Boltzmann distribution is $\sqrt{<v>^2} = \sqrt{\frac{3k_B T}{m_e^*}}$, which can be seen as an estimated electron velocity, p/m_e^*, and thus

$$\lambda = \frac{h}{\sqrt{3m_e^* k_B T}} \ .$$ (6.2)

If an electron and a hole enter within distance λ of each other, then a check is made whether there will be recombination. To do that firstly we calculate the reduced mass,

$$\mu = \frac{m_e^* m_h^*}{m_e^* + m_h^*} \ ,$$ (6.3)

and then the difference in kinetic energy of the electron-hole pair and their binding energy

$$E_b = \left(m_e^* + m_h^*\right) v_{cm}^2 - \frac{\mu e^4}{\epsilon_0^2 h^2 \pi^2} \ ,$$ (6.4)

where v_{cm} is the center of mass velocity of the electron-hole pair. If $E_b < 0$ it means that the pair's kinetic energy is larger than the binding energy and no recombination occurs. If the opposite is true, a recombination occurs and both particles are removed from the simulation. Although in a real case scenario the difference in energies will be given off as thermal energy, in our simulation this is not done.
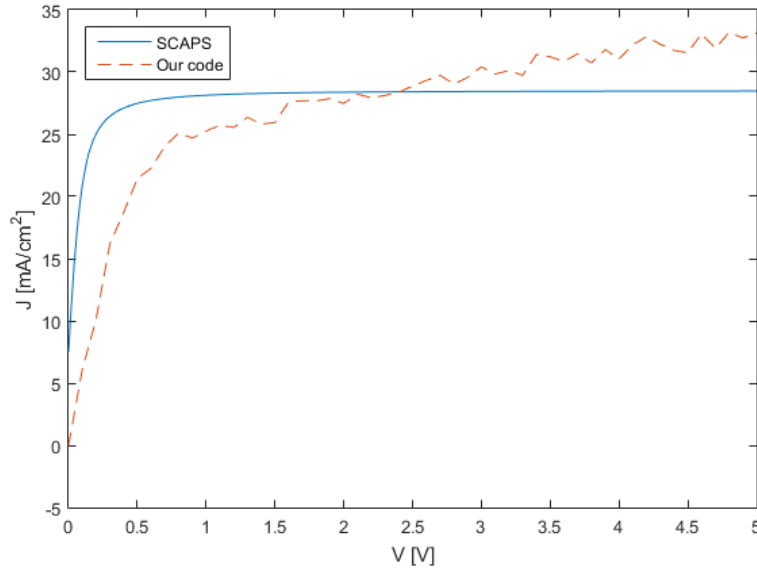
Figure 6.3: Preliminary results for thin film silicon solar cells compared with the SCAPS software [71].

As an initial test, the results of our molecular dynamics simulations have been compared to the results of the SCAPS (a Solar Cell Capacitance Simulator) code for a p-n silicon junction of $d = 10$ microns. The SCAPS code solves self-consistently the drift-diffusion equations for solar cells of up to six material layers [71]. A comparison of some preliminary results can be seen in Fig. 6.3. The figure shows the current density as a function of applied voltage obtained with SCAPS and with our molecular dynamics code [72].

6.2   Inertial hysteresis

For further testing purposes the cell was connected to variable voltage and the dynamic I-V characteristic was explored. A hysteresis of the current was expected due to the non-zero masses of the carriers and also due to the space-charge distribution. The hysteresis is in fact a phase shift between the voltage and the current.

The generic equation of motion of a particle of charge q, mass m, and mobility μ, in a constant (uniform) electric field E is

$$m\ddot{x} = qE - \frac{q}{\mu}\dot{x} \,, \tag{6.5}$$

where the last term corresponds to a friction force proportional to the velocity. Given the initial position x_0 and initial velocity v_0 the equation is easily integrated. The solution for the velocity can be written as

$$v(t) = v_0 e^{-t/\tau} + \mu E \left(1 - e^{-t/\tau}\right) \,, \tag{6.6}$$

where $\tau = \mu m/q$ can be interpreted as the relaxation time for the velocity, i. e. the characteristic time until the velocity reaches the steady-state value μE in a constant electric field. In a time periodic electric field, $E = E_0 \sin(\omega t)$, with period $T = 2\pi/\omega$, one expects a phase shift between the current (essentially given by the velocity) and the voltage (field) corresponding to $\omega\tau$. Using the effective masses of electrons and holes in silicon, $m_e^* = 0.19 m_0$ and $m_h^* = 0.49 m_0$, and their mobilities $\mu_e = 0.14$ m^2/Vs and $\mu_h = 0.045$ m^2/Vs, one obtains $\tau_e = 0.15$ ps an $\tau_h = 0.13$ ps. Therefore a significant (or relevant) I-V hysteresis is expected if the period of the time-periodic field is about 5-10 ps or lower, such that $\omega\tau \sim 0.1$ rad.

We used a sinusoidal signal with period of 100 ps and variable amplitude with values of $V_c = 0.6, 5, 10, 20, 40$ and 80 V. We can see the hysteresis in all plots of Fig. 6.4 although with some differences from what one expects from the simple analysis shown above. The I-V characteristic are in fact Lissajous figures. The horizontal lines should be interpreted as numerical out-layers of the velocities of the carriers. As electron-hole pairs are created they are assigned random velocities. If these velocities are very large they can create spikes in the Ramo-Shockley current and that might be what we are seeing here. Further investigations are to be done.

For the lowest voltage the obtained phase shift of about 0.4 rad, i. e. considerably larger than the single-particle prediction. The reason is the effect of the charge distribution which contributes to the total electric field acting on each carrier. The total field has itself a specific time constant which is difficult to derive analytically due to the complex many-body aspects, but it can be inferred from the numerical calculations. The typical number of electrons and holes in the diode was of several hundreds.

For higher voltages more complicated loops can form. The reason is that with increasing the voltage the higher harmonics of the current can be activated, i. e. the current becomes a Fourier series like

$$i(t) = \sum_{n\geq 1} i_n \sin(n\omega t + \phi_n) \,, \tag{6.7}$$

where the coefficients of higher harmonics i_n depend on the higher powers of the voltage amplitude, i. e. the nonlinear effects become important. At the same time the randomness of the velocities play an increasing role with increasing the voltage amplitude.
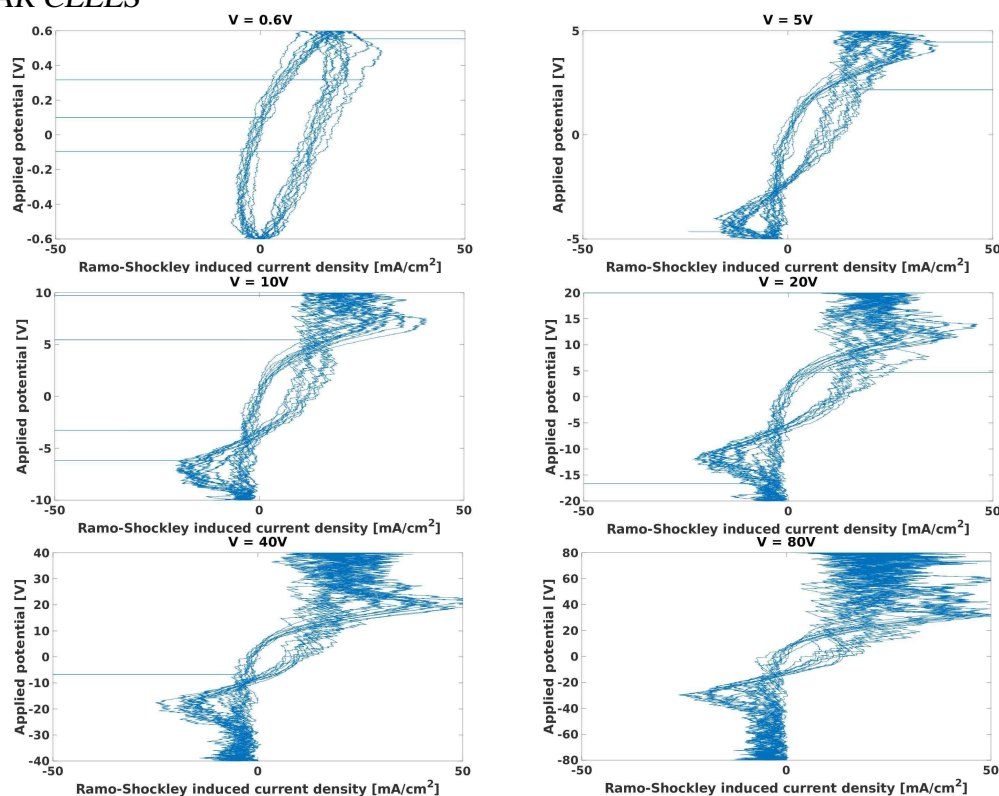
Figure 6.4: Hysteresis loops of time periodic voltage and current in a silicon solar cell.

6.3 The effect of molecular dipoles in hybrid organic-inorganic solar cells

A new generation of solar cells emerged over the last few years consisting in light harvesting regions based on hybrid organic-inorganic materials. One example is $CH_3NH_3PbI_3$ perovskites, Fig. 6.5. The advantage over the silicon cells is that they are much cheaper than the silicon p-n junctions, and much easier to obtain in the lab [73]–[75]. Their photoconversion efficiency is up to 20%, which is considered very good compared with silicon, which is typically of 30-45%. They do not require a pure crystalline phase, since they are essentially disordered materials, and do not need doping. A solar cell needs an internal electric field which must spread the electron and the hole once they are created by a photon. Otherwise the electron and the hole recombine. In a classical silicon p-n junction this field is produced over several hundreds of nanometers, in the interface region between the n-doped and p-doped sides of the junction. In the $CH_3NH_3PbI_3$ perovskite structure the methylammonium molecules H_3NH_3 have dipole moments that permanently rotate inside the PbI_3 cage [76]. It is believed that these dipole moments are responsible for separating the electrons and the holes shortly after they are created. It is also believed that the $CH_3NH_3PbI_3$ perovskites can have ferroelectric domains where the dipole moments are all aligned in the same directions [77].

In order to adapt our simulations to such type of materials we included in the diode a number of electrical dipole moments. They are allowed to rotate and align with the total local electric field in order to minimize their energy. The field created by each dipole is included in the total electric field calculated in each region of the diode where carriers or dipoles reside.
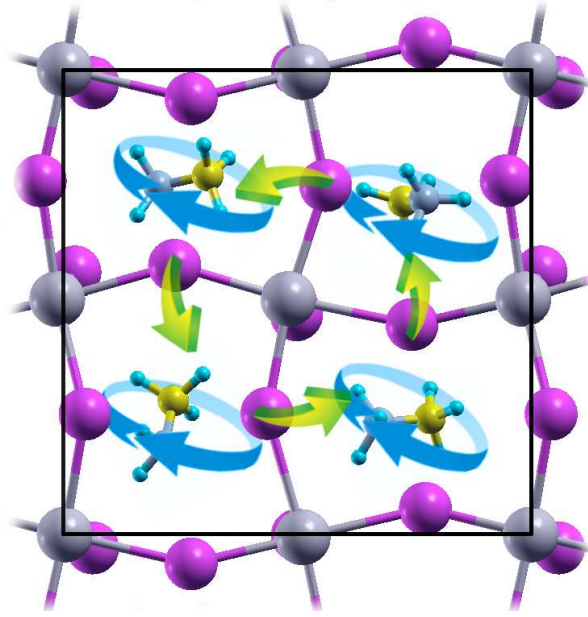
Figure 6.5: The perovskite structure of $CH_3NH_3PbI_3$. In the center of each of the four cells displayed is the methylammonium polar molecule CH_3NH_3, which rotates due to thermal energy and electric field. The Pb atoms are shown in grey and the I atoms in pink [76].

The alignment is modeled using a Monte Carlo method familiar in statistical mechanics and the Boltzmann distribution. Ait each time step of the molecular dynamics simulation a new position and orientation for each dipole is decided by calculating the Boltzmann factor

$$\frac{F(State2)}{F(State1)} = e^{\frac{U_1 - U_2}{k_B T}} \; , \tag{6.8}$$

where U_1 and U_2 are potential energies is states 1 and 2. A Metropolis–Hastings algorithm is used to determine if a dipole will rotate or not. In the present implementation the dipoles are treated as points and their electric field is calculated in the long range limit with the formula

$$\mathbf{E}(\mathbf{R}) = \frac{3(\mathbf{p} \cdot \hat{\mathbf{R}})\hat{\mathbf{R}} - \mathbf{p}}{4\pi\varepsilon R^3} \; . \tag{6.9}$$

With this addition of internal dipoles, and with the corresponding material parameters of the halide perovskite $CH_3NH_3PbI_3$, $m_e^* = 0.23m_0$ and $m_h^* = 0.29m_0$, and their mobilities $\mu_e = 2.0 \text{ m}^2/\text{V}s$ and $\mu_h = 2.0 \text{ m}^2/\text{V}s$, $E_g = 1.55$ eV, we repeated the dynamic simulations of the I-V characteristics of a 10 micron thick halide-perovskite layer. The single-particle velocity relaxation is now one order of magnitude larger that for silicon, because of the increased mobilities, i. e. $\tau_e = 2.6$ ps and $\tau_h = 3.3$ ps. The dipole moment of the methylammonium molecule is taken as 2.1 Debye.

In the first series of simulations we did not include dipoles, Fig. 6.6. The calculations are done for a periodic voltage of amplitude 1 and 10 V, of period 10 and 100 ps. This time we also show the time periodic current, together with the partial electron and hole components. Let's observe first that the partial currents are not symmetric relatively to zero values. The reason is that the absorption of the photons is done at one side of the cell, near the anode, as illustrated in Fig. 6.2. This is a realistic situation, since the photons enter into the device through a phototransparent oxide usually made of TiO2, which also serves as electron transport material. At the other end of the device a hole transporter organic material called Spiro-MeOTAD is usually attached [75]. However the hole transporter is not really

necessary and sometimes it also creates serious degradation of the device in time [78]. In our simplified device model the electrons are absorbed at the right boundary of the diode and the holes at the left boundary, Fig. 6.6, with equal probabilities. Further developments of the model will include the effect of band alignment between the electron/hole transporters and the halide perovskite [79].

For comparison, next figure, 6.7, show the results for the same simulation parameters, but with the incident photons uniformly distributed in the volume of the halide perovskite. There are small and non-significant, differences between the hysteresis loops obtained for the same period and voltage in the nonuniform and uniform cases. As before, in the case of silicon, we obtain a hysteresis at periods one order of magnitude larger than the characteristic velocity relaxation time, due to the space charge distribution. However the Coulomb effects seem to be weaker in the halide perovskite, where the dielectric constant is 25.7, compared to silicon, with dielectric constant more than two times smaller, 11.7. Increasing the voltage the hysteresis become more prominent and higher harmonics of the current manifest as additional loops.

In the next examples we included the dipole moments. A number of 125 dipoles were distributed in the volume, i. e. $5 \times 5 \times 5$ in the three spatial directions, respectively, randomly oriented. In order to mimic macroscopic ferroelectric domains the magnitude of each dipole has been multiplied with a factor 10^6, Fig. 6.8. No significant changes can be seen in the presence of the dipoles. Further amplifying the dipoles by a factor of 10^{10}, we see that the noise of the currents increases, Fig. 6.9. This is understandable, since carriers situated close to a dipole can be strongly accelerated.

Hence, our results show that the inertial hysteresis survives in the presence of the intrinsic dipole moments existent in the halide perovskite materials. The dipoles or ferroelectric domains have indeed their own dynamics. They can change orientation due to the flip of the input voltage. But their characteristic times are much larger than the carrier velocity times. The dipole relaxation times essentially depend on the mass of the molecular dipoles, which is orders of magnitude larger than the mass of the carriers. Therefore the hysteresis due to rotation of dipoles occurs at much lower frequencies, of the order of Hertz or in the static limit, although the halide perovskites are considered weak ferroelectrics [80], [81]. However the origin of the hysteresis phenomenon in these materials is a hot research topic, since the phenomenon has also been attributed to other causes, like charge trapping or charge migration, of electronic or ionic nature [82]. Most likely the hysteretic behavior is a result of several mechanisms of electric polarization, each one with a specific relaxation time, which in the end contribute to the degradation or ageing of the solar cell. The inertial mechanism presented in this thesis has probably the shortest relaxation time. Other mechanisms are being incorporated in the molecular dynamics code developed at the Nanophysics Center of Reykjavik University within a separate project on space charge dynamics in halide-perovskite materials [72].
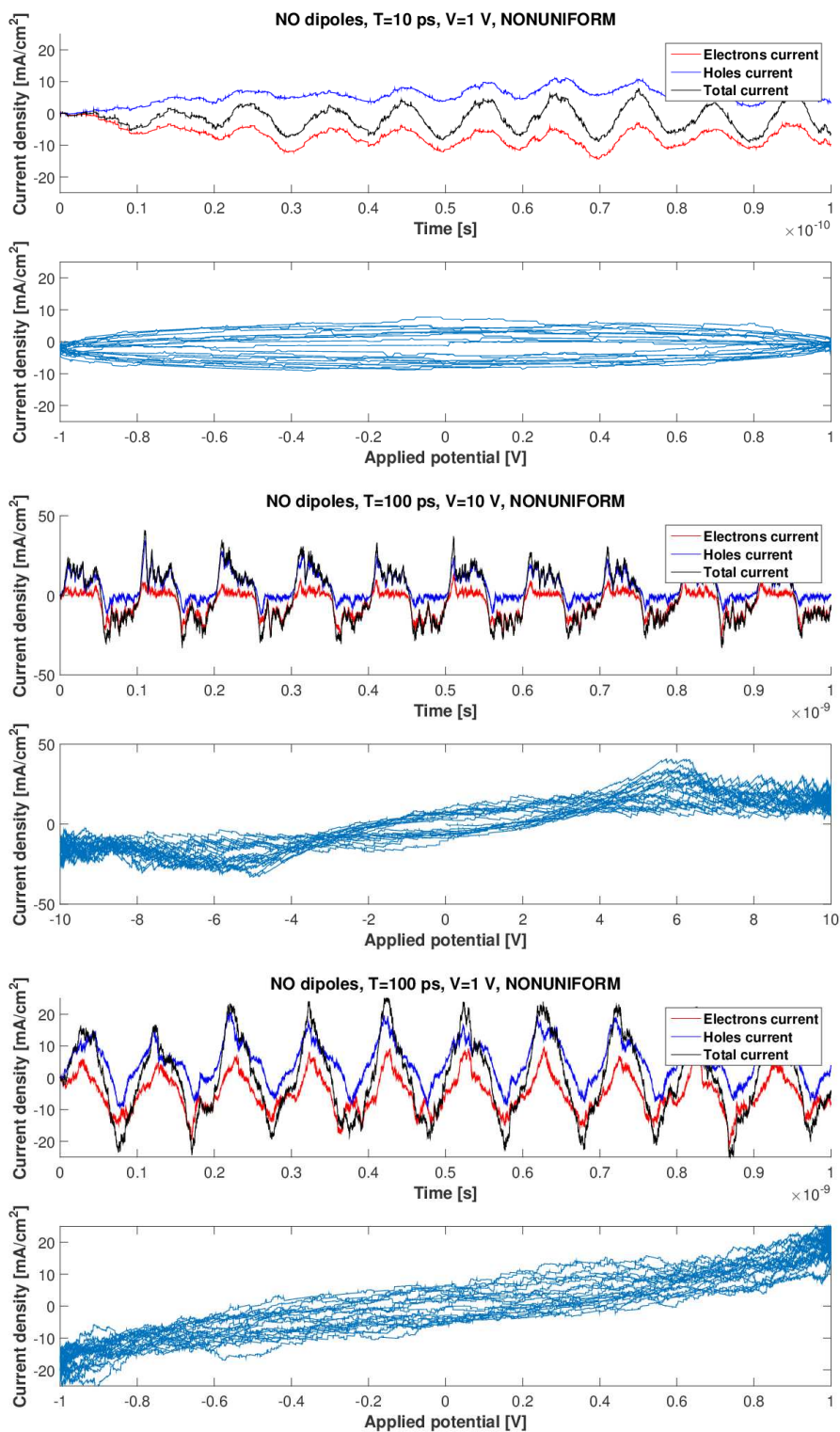
Figure 6.6: Dynamic hysteresis in methylammonium halide perovskite without dipoles. The photon flux is entering the diode from the right lateral surface, as shown in Fig. 6.2.
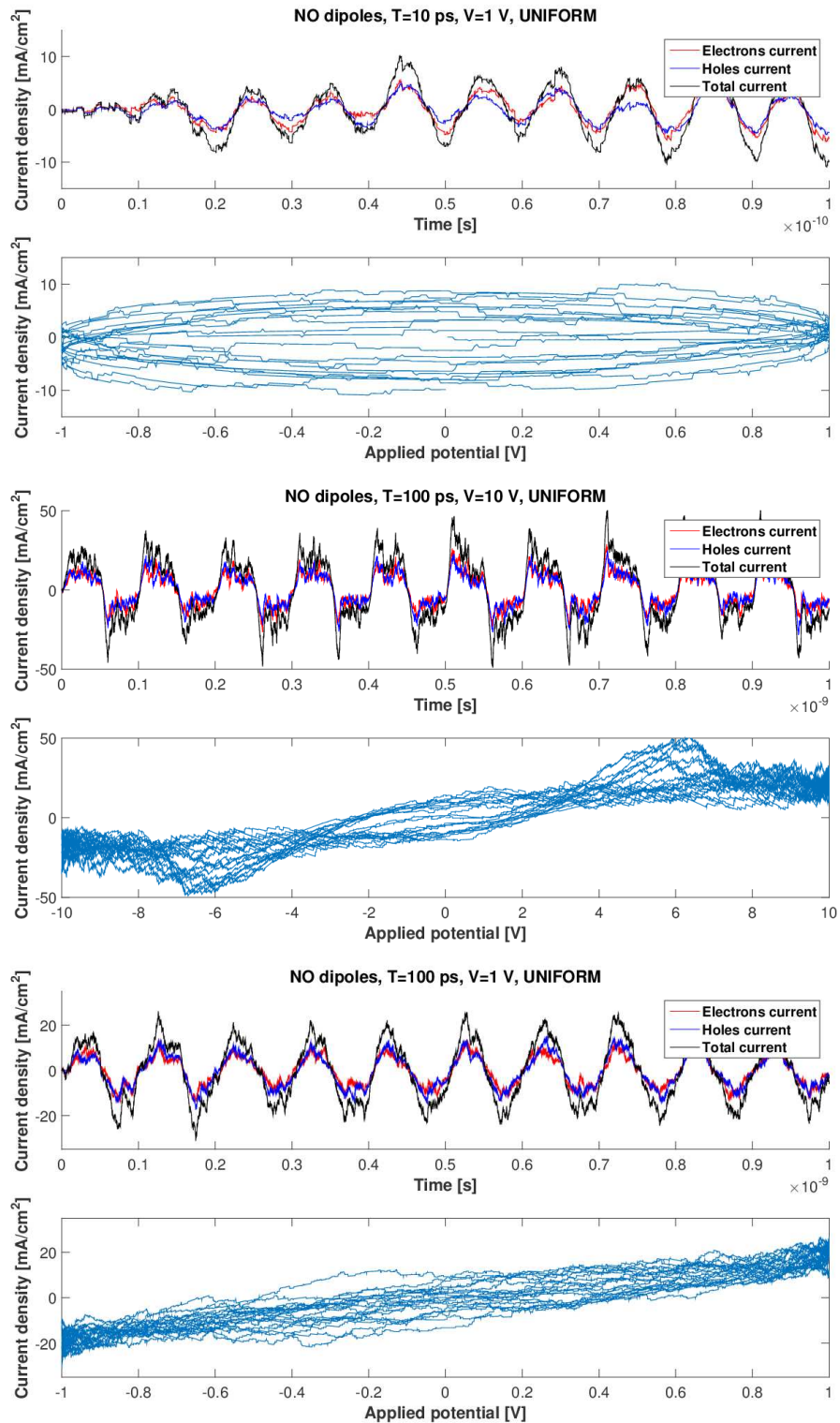
Figure 6.7: Dynamic hysteresis in methylammonium halide perovskite without dipoles. The photon flux is uniform in the volume of the diode.

Figure 6.8: Dynamic hysteresis in methylammonium halide perovskite with 125 dipoles magnified 10^6 times. The photon flux is entering the diode from the right lateral surface, as shown in Fig. 6.2.

Figure 6.9: Dynamic hysteresis in methylammonium halide perovskite with 125 dipoles magnified 10^{10} times. The photon flux is entering the diode from the right lateral surface, as shown in Fig. 6.2.
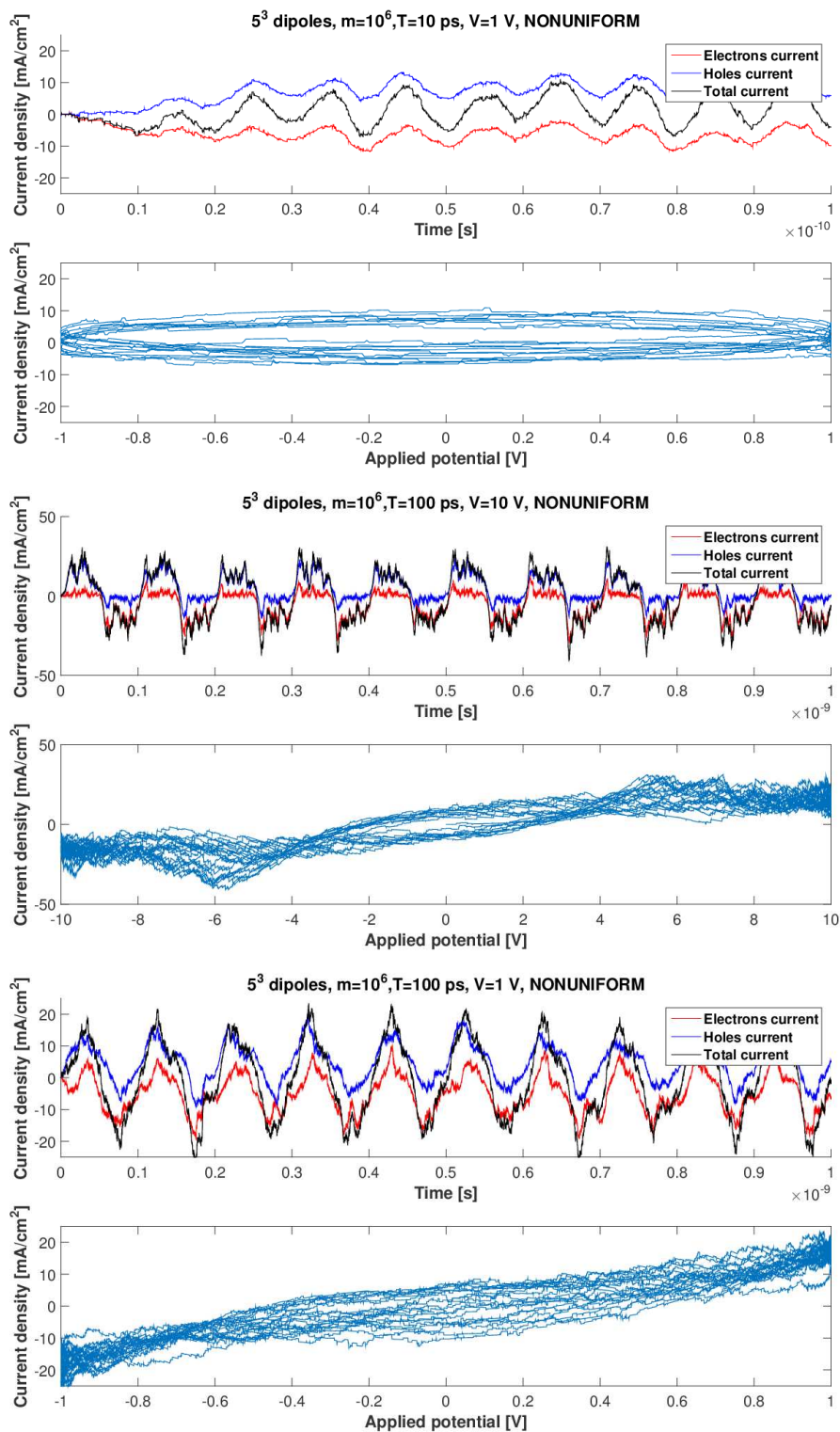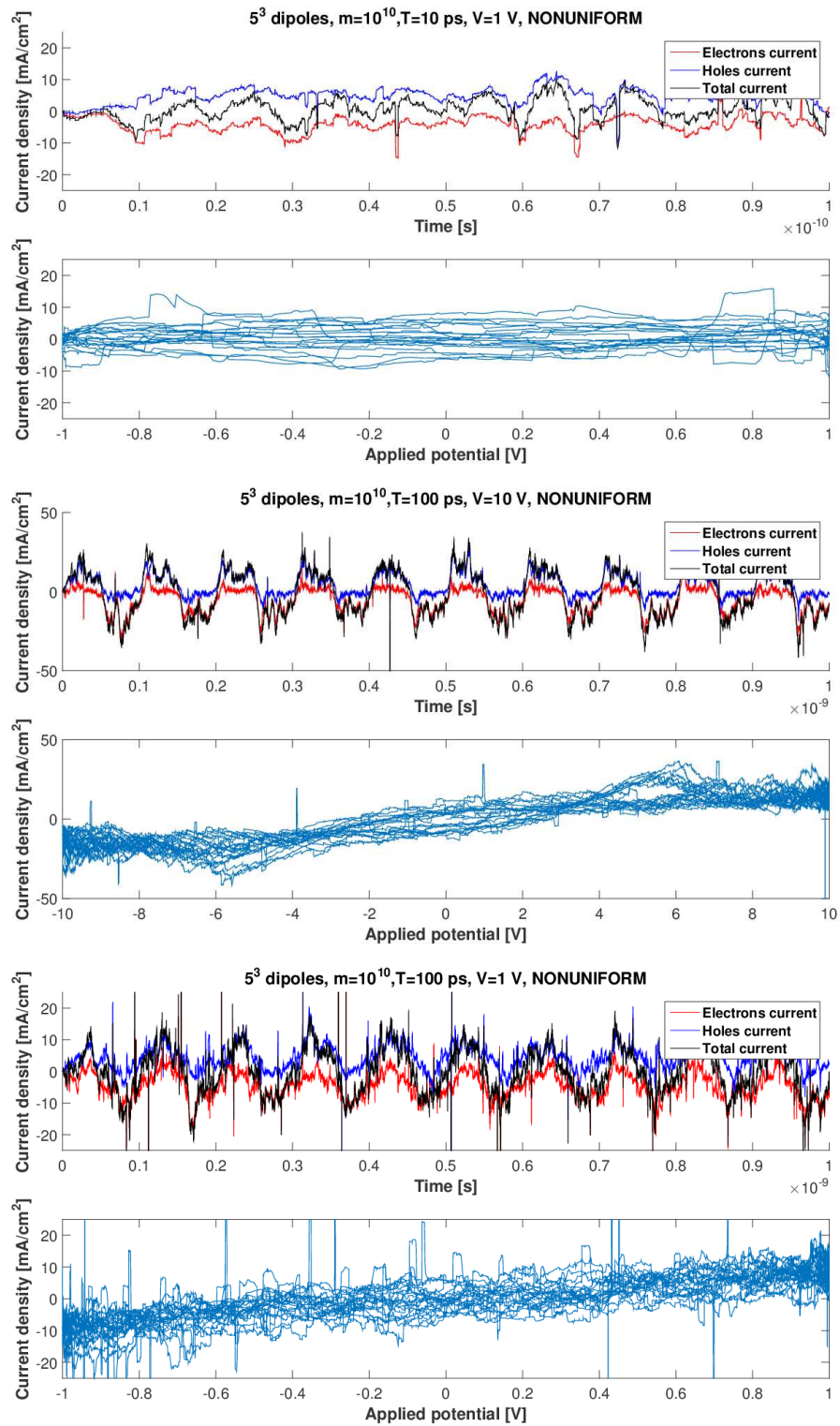
Chapter 7

Conclusions

THz radiation has already proven as a valuable asset to science and technology. THz imaging, THz spectroscopy, GB/s wireless communication [83], to name a few. Sources of this radiation band have a lot of unresolved issues. The ones that do produce THz radiation are the free electron lasers, and they require dedicated facilities and teams of scientists and engineers. The vacuum electronic devices do work well but they can be extremely large and expensive. Solid state devices can be small but have a low maximum of obtainable frequencies because the transit time of the charge carriers within the device cannot be decreased indefinitely. Obviously problems exist and persist all over the map but also do opportunities which drive the progress in this very young field.

We have shown in our work that such devices are possible by combining the speed of free electron sources and the miniature dimensions of a solid state device. The proposed diode can have a frequency band of operation based on its radius and through the voltage it can be tuned to change the frequency within this band continuously. Although these devices, due to their miniature dimensions would produce power in the order of tens of μW, putting them in arrays can increase their power coherently. One way was to have them placed near to each other and their respective electron beams interacting with their nearest neighbors. Such a device would increase the power tenfold but also would introduce a lot of noise. Investigations were made on such arrays with each emitter having multiple bunches of its own in front of it. Further investigations showed that having one bunch only in front of each emitter would decrease the noise for one emitter but also in this configuration would cause the emitters to work in anti-phase or against each other.

We made a proposal to have a similar array of emitters where the emitters are far enough from each other, that they don't interact. Then into the gap voltage, a signal from one lone single emitter is fed. The small voltage created by this one emitter would cause all other emitters to submit to it and follow it's beat. This is a well known configuration in physics. This way, many of the problems from the previously shown interacting arrays should be decreased (noise and frequency reduction). An initial code was written for this particular problem, but further studies need to be done.

We made investigations into the non-zero initial velocity of the emitted electrons. Until this point, all simulations were run for zero initial velocity, which can correspond to T=0K, and that is nonphysical. Increased initial velocities corresponding to Maxwell-Boltzmann distributions of up to T=300K were included and all of them gave promising results for single emitters.

Finally, within a preliminary study of charge dynamics in solar cells, using the methodology of molecular dynamics extended to electrons and holes, we predict an inertial dynamical mechanism for hysteresis in solar cells, at high frequencies such as GHz. More work needs

to be done in this direction to incorporate in the code realistic parameters regarding dipole moments, specific to halide perovkite materials, generation and recombination rates, and absorption of carriers by the electron and hole transporter layers.

Bibliography

[1]   P. H. Siegel *et al.*, "Terahertz technology", *IEEE Transactions on microwave theory and techniques*, vol. 50, no. 3, pp. 910–928, 2002.

[2]   P. H. Siegel, "Terahertz technology in biology and medicine", in *Microwave Symposium Digest, 2004 IEEE MTT-S International*, IEEE, vol. 3, 2004, pp. 1575–1578.

[3]   J. H. Booske, "Plasma physics and related challenges of millimeter-wave-to-terahertz and high power microwave generationa)", *Physics of Plasmas (1994-present)*, vol. 15, no. 5, p. 055 502, 2008.

[4]   J. H. Booske, R. J. Dobbs, C. D. Joye, C. L. Kory, G. R. Neil, G.-S. Park, J. Park, and R. J. Temkin, "Vacuum electronic high power terahertz sources", *Terahertz Science and Technology, IEEE Transactions on*, vol. 1, no. 1, pp. 54–75, 2011.

[5]   G. Scalari, C. Walther, M. Fischer, R. Terazzi, H. Beere, D. Ritchie, and J. Faist, "Thz and sub-thz quantum cascade lasers", *Laser & Photonics Reviews*, vol. 3, no. 1-2, pp. 45–66, 2009.

[6]   M. Tonouchi, "Cutting-edge terahertz technology", *Nature photonics*, vol. 1, no. 2, pp. 97–105, 2007.

[7]   B. S. Williams, "Terahertz quantum-cascade lasers", *Nature photonics*, vol. 1, no. 9, pp. 517–525, 2007.

[8]   P. U. Jepsen, D. G. Cooke, and M. Koch, "Terahertz spectroscopy and imaging–modern techniques and applications", *Laser & Photonics Reviews*, vol. 5, no. 1, pp. 124–166, 2011.

[9]   J. Federici and L. Moeller, "Review of terahertz and subterahertz wireless communications", *Journal of Applied Physics*, vol. 107, no. 11, p. 111 101, 2010.

[10] A. Y. Pawar, D. D. Sonawane, K. B. Erande, and D. V. Derle, "Terahertz technology and its applications", *Drug Invention Today*, vol. 5, no. 2, pp. 157–163, 2013.

[11] C. Sirtori, "Applied physics: Bridge for the terahertz gap", *Nature*, vol. 417, no. 6885, pp. 132–133, 2002.

[12] R. Köhler, A. Tredicucci, F. Beltram, H. E. Beere, E. H. Linfield, A. G. Davies, D. A. Ritchie, R. C. Iotti, and F. Rossi, "Terahertz semiconductor-heterostructure laser", *Nature*, vol. 417, no. 6885, pp. 156–159, 2002.

[13] G. Févotte, "New perspectives for the on-line monitoring of pharmaceutical crystallization processes using in situ infrared spectroscopy", *International journal of pharmaceutics*, vol. 241, no. 2, pp. 263–278, 2002.

[14] R. M. Woodward, V. P. Wallace, R. J. Pye, B. E. Cole, D. D. Arnone, E. H. Linfield, and M. Pepper, "Terahertz pulse imaging of ex vivo basal cell carcinoma", *Journal of Investigative Dermatology*, vol. 120, no. 1, pp. 72–78, 2003.

[15] E. Berry, J. W. Handley, A. J. Fitzgerald, W. Merchant, R. D. Boyle, N. Zinov'ev, R. E. Miles, J. M. Chamberlain, and M. A. Smith, "Multispectral classification techniques for terahertz pulsed imaging: An example in histopathology", *Medical engineering & physics*, vol. 26, no. 5, pp. 423–430, 2004.

[16] C. Bower, D. Shalom, W. Zhu, D. López, G. P. Kochanski, P. L. Gammel, and S. Jin, "A micromachined vacuum triode using a carbon nanotube cold cathode", *Electron Devices, IEEE Transactions on*, vol. 49, no. 8, pp. 1478–1483, 2002.

[17] C. Bower, W. Zhu, D. Shalom, D. Lopez, L. Chen, P. Gammel, and S. Jin, "On-chip vacuum microtriode using carbon nanotube field emitters", *Applied physics letters*, vol. 80, no. 20, pp. 3820–3822, 2002.

[18] P. Siegel, A. Fung, M. Manohara, J. Xu, and B. Chang, "Nanoklystron: A monolithic tube approach to thz power generation", in *Proceedings of the 12th international Symposium on Space Terahertz technology*, Natioanl Radio Astronomy Observatory, 2001, pp. 81–90.

[19] S. Bhattacharjee, J. H. Booske, C. L. Kory, D. W. van der Weide, S. Limbach, S. Gallagher, J. D. Welter, M. R. Lopez, R. M. Gilgenbach, R. L. Ives, *et al.*, "Folded waveguide traveling-wave tube sources for terahertz radiation", *Plasma Science, IEEE Transactions on*, vol. 32, no. 3, pp. 1002–1014, 2004.

[20] O. W. Richardson, *The emission of electricity from hot bodies*. Longmans, Green and Company, 1921.

[21] R. H. Fowler and L. Nordheim, "Electron emission in intense electric fields", in *Proceedings of the Royal Society of London A: Mathematical, Physical and Engineering Sciences*, The Royal Society, vol. 119, 1928, pp. 173–181.

[22] R. H. Fowler, "The analysis of photoelectric sensitivity curves for clean metals at various temperatures", *Physical Review*, vol. 38, no. 1, p. 45, 1931.

[23] L. A. DuBridge, "A further experimental test of fowler's theory of photoelectric emission", *Physical Review*, vol. 39, no. 1, p. 108, 1932.

[24] ——, "Theory of the energy distribution of photoelectrons", *Physical Review*, vol. 43, no. 9, p. 727, 1933.

[25] K. L. Jensen, "Electron emission physics", *Advances in Imaging and Electron Physics*, vol. 149, pp. 147–279, 2007.

[26] K. L. Jensen, P. G. O'Shea, and D. W. Feldman, "Generalized electron emission model for field, thermal, and photoemission", *Applied physics letters*, vol. 81, no. 20, pp. 3867–3869, 2002.

[27] J. Luginsland, Y. Lau, R. Umstattd, and J. Watrous, "Beyond the child–langmuir law: A review of recent results on multidimensional space-charge-limited flow", *Physics of Plasmas (1994-present)*, vol. 9, no. 5, pp. 2371–2376, 2002.

[28] L. K. Ang, W. Koh, Y. Lau, and T. Kwan, "Space-charge-limited flows in the quantum regimea)", *Physics of Plasmas (1994-present)*, vol. 13, no. 5, p. 056 701, 2006.

[29] L. Ang, T. Kwan, and Y. Lau, "New scaling of child-langmuir law in the quantum regime", *Physical review letters*, vol. 91, no. 20, p. 208 303, 2003.

[30] Y. Zhu and L. Ang, "Child–langmuir law in the coulomb blockade regime", *Applied Physics Letters*, vol. 98, no. 5, p. 051 502, 2011.

[31] A. Valfells, D. Feldman, M. Virgo, P. O'shea, and Y. Lau, "Effects of pulse-length and emitter area on virtual cathode formation in electron guns", *Physics of Plasmas (1994-present)*, vol. 9, no. 5, pp. 2377–2382, 2002.

[32] Y. Lau, "Simple theory for the two-dimensional child-langmuir law", *Physical review letters*, vol. 87, no. 27, p. 278 301, 2001.

[33] L. Ang and P. Zhang, "Ultrashort-pulse child-langmuir law in the quantum and relativistic regimes", *Physical review letters*, vol. 98, no. 16, p. 164 802, 2007.

[34] Y. Feng and J. Verboncoeur, "Transition from fowler-nordheim field emission to space charge limited current density", *Physics of Plasmas (1994-present)*, vol. 13, no. 7, p. 073 105, 2006.

[35] A. Rokhlenko, K. L. Jensen, and J. L. Lebowitz, "Space charge effects in field emission: One dimensional theory", *Journal of Applied Physics*, vol. 107, no. 1, p. 014 904, 2010.

[36] K. Torfason, A. Valfells, and A. Manolescu, "Molecular dynamics simulations of field emission from a planar nanodiode", *Physics of Plasmas (1994-present)*, vol. 22, no. 3, p. 033 109, 2015.

[37] P. Akimov, H. Schamel, H. Kolinsky, A. Y. Ender, and V. Kuznetsov, "The true nature of space-charge-limited currents in electron vacuum diodes: A lagrangian revision with corrections", *Physics of Plasmas*, vol. 8, pp. 3788–3798, 2001.

[38] R. Caflisch and M. Rosin, "Beyond the child-langmuir limit", *Physical Review E*, vol. 85, no. 5, p. 056 408, 2012.

[39] M. Griswold, N. Fisch, and J. Wurtele, "An upper bound to time-averaged space-charge limited diode currents", *Physics of Plasmas (1994-present)*, vol. 17, no. 11, p. 114 503, 2010.

[40] Y. Zhu, P. Zhang, A. Valfells, L. Ang, and Y. Lau, "Novel scaling laws for the langmuir-blodgett solutions in cylindrical and spherical diodes", *Physical review letters*, vol. 110, no. 26, p. 265 007, 2013.

[41] R. J. Barker, N. C. Luhmann, J. H. Booske, and G. S. Nusinovich, "Modern microwave and millimeter-wave power electronics", *Modern Microwave and Millimeter-Wave Power Electronics, by Robert J. Barker (Editor), Neville C. Luhmann (Editor), John H. Booske (Editor), Gregory S. Nusinovich, pp. 872. ISBN 0-471-68372-8. Wiley-VCH, April 2005.*, vol. 1, 2005.

[42] R. S. Symons, "Tubes: Still vital after all these years", *Spectrum, IEEE*, vol. 35, no. 4, pp. 52–63, 1998.

[43] Y.-M. Shin, L. R. Barnett, D. Gamzina, N. C. Luhmann Jr, M. Field, and R. Borwick, "Terahertz vacuum electronic circuits fabricated by uv lithographic molding and deep reactive ion etching", *Applied Physics Letters*, vol. 95, no. 18, p. 181 505, 2009.

[44] W. Zhu, *Vacuum microelectronics*. John Wiley & Sons, 2001.

[45] R. L. Ives, "Microfabrication of high-frequency vacuum electron devices", *Plasma Science, IEEE Transactions on*, vol. 32, no. 3, pp. 1277–1291, 2004.

[46] A. Pedersen, A. Manolescu, and A. Valfells, *Phys. Rev. Lett*, vol. 104, p. 175 002, 2010.

[47] C. K. Birdsall, *Electron dynamics of diode regions*. Elsevier, 1966.

[48] A. Valfells, D. Feldman, M. Virgo, P. O'shea, and Y. Lau, "Effects of pulse-length and emitter area on virtual cathode formation in electron guns", *Physics of Plasmas (1994-present)*, vol. 9, no. 5, pp. 2377–2382, 2002.

[49] P. Jonsson, M. Ilkov, A. Manolescu, A. Pedersen, and A. Valfells, *Physics of Plasmas*, vol. 20, p. 023 107, 2013.

[50] L. Ang, Y. Lau, and T. Kwan, "Simple derivation of quantum scaling in child-langmuir law", *Plasma Science, IEEE Transactions on*, vol. 32, no. 2, pp. 410–412, 2004.

[51] J. Luginsland, Y. Lau, and R. Gilgenbach, "Two-dimensional child-langmuir law", *Physical review letters*, vol. 77, no. 22, p. 4668, 1996.

[52] J. M. Dawson, "Particle simulation of plasmas", *Rev. Mod. Phys.*, vol. 55, pp. 403–447, 2 Apr. 1983.

[53] H. Grubmüller, H. Heller, A. Windemuth, and K. Schulten, "Generalized verlet algorithm for efficient molecular dynamics simulations with long-range interactions", *Molecular Simulation*, vol. 6, no. 1-3, pp. 121–142, 1991.

[54] E. Hairer, C. Lubich, and G. Wanner, "Geometric numerical integration illustrated by the störmer–verlet method", *Acta numerica*, vol. 12, pp. 399–450, 2003.

[55] D. Marx and J. Hutter, *Ab initio molecular dynamics: Basic theory and advanced methods*. Cambridge University Press, 2009.

[56] A. Pikovsky, M. Rosenblum, and J. Kurths, *Syncronization*. Mc.Graw Hill, May 2003.

[57] B. Kralemann, L. Cimpoieriu, M. Rosenblum, A. Pikovsky, and R. Mrowka, *Phys. Rev. E*, vol. 77, p. 066 205, 2008.

[58] B. Ragan-Kelley, J. Verboncoeur, and Y. Feng, "Two-dimensional axisymmetric child–langmuir scaling law", *Physics of Plasmas (1994-present)*, vol. 16, no. 10, p. 103 102, 2009.

[59] K. L. Jensen and E. J. Montgomery, "Photoemission theory and the development of high performance photocathodes", *Journal of Computational and Theoretical Nanoscience*, vol. 6, no. 8, pp. 1754–1769, 2009.

[60] K. L. Jensen, N. Moody, D. Feldman, E. Montgomery, and P. O'Shea, "Photoemission from metals and cesiated surfaces", *Journal of Applied Physics*, vol. 102, no. 7, p. 074 902, 2007.

[61] D. H. Dowell and J. F. Schmerge, "Quantum efficiency and thermal emittance of metal photocathodes", *Physical Review Special Topics-Accelerators and Beams*, vol. 12, no. 7, p. 074 201, 2009.

[62] S. Neppl, "Attosecond time-resolved photoemission from surfaces and interfaces", PhD thesis, Universität München, 2012.

[63] K. L. Jensen, P. O'Shea, and D. Feldman, "Emittance of a photocathode: Effects of temperature and field", *Physical Review Special Topics-Accelerators and Beams*, vol. 13, no. 8, p. 080 704, 2010.

[64] K. L. Jensen, J. Lebowitz, Y. Lau, and J. Luginsland, "Space charge and quantum effects on electron emission", *Journal of Applied Physics*, vol. 111, no. 5, p. 054 917, 2012.

[65] K. L. Jensen, D. A. Shiffler, J. J. Petillo, Z. Pan, and J. W. Luginsland, "Emittance, surface structure, and electron emission", *Physical Review Special Topics-Accelerators and Beams*, vol. 17, no. 4, p. 043 402, 2014.

[66] I. Langmuir, "The effect of space charge and residual gases on thermionic currents in high vacuum", *Phys. Rev.*, vol. 2, pp. 450–486, 6 Dec. 1913. DOI: `10.1103/PhysRev.2.450`. [Online]. Available: `http://link.aps.org/doi/10.1103/PhysRev.2.450`.

[67] C. Gueymard, D. Myers, and K. Emery, "Proposed reference irradiance spectra for solar energy systems testing", *Solar energy*, vol. 73, no. 6, pp. 443–467, 2002.

[68] B. G. Streetman and S. Banerjee, *Solid state electronic devices*. Prentice Hall New Jersey, 2000, vol. 4.

[69] W. Shockley, "Currents to conductors induced by a moving point charge", *Journal of Applied Physics*, vol. 9, no. 10, pp. 635–636, 1938.

[70] S. Ramo, "Currents induced by electron motion", *Proc. Ire*, vol. 27, no. 9, pp. 584–585, 1939.

[71] M. Burgelman, P. Nollet, and S. Degrave, "Modelling polycrystalline semiconductor solar cells", *Thin Solid Films*, vol. 361–362, pp. 527–532, 2000.

[72] K. Torfason, "Charge transport in perovskites", [Online]. Available: `http://nano.ru.is/`.

[73] M. M. Lee, J. Teuscher, T. Miyasaka, T. N. Murakami, and H. J. Snaith, "Efficient hybrid solar cells based on meso-superstructured organometal halide perovskites", *Science*, vol. 338, no. 6107, pp. 643–647, 2012.

[74] J. H. Heo, S. H. Im, J. H. Noh, T. N. Mandal, C.-S. Lim, J. A. Chang, Y. H. Lee, H.-j. Kim, A. Sarkar, N. K., M. Gratzel, and S. I. Seok, "Efficient inorganic-organic hybrid heterojunction solar cells containing perovskite compound and polymeric hole conductors", *Nat. Photon*, vol. 7, no. 6, pp. 486–491, 2013.

[75] M. Grätzel, "The light and shade of perovskite solar cells", *Nat. Mater.*, vol. 13, no. 9, pp. 838–842, 2014.

[76] C. Goehry, G. A. Nemnes, and A. Manolescu, "Collective behavior of molecular dipoles in ch3nh3pbi3", *The Journal of Physical Chemistry C*, vol. 119, no. 34, pp. 19 674–19 680, 2015.

[77] J. M. Frost, K. T. Butler, F. Brivio, C. H. Hendon, M. van Schilfgaarde, and A. Walsh, "Atomistic origins of high-performance in hybrid halide perovskite solar cells", *Nano Letters*, vol. 14, no. 5, pp. 2584–2590, 2014.

[78] E. Edri, S. Kirmayer, A. Henning, S. Mukhopadhyay, K. Gartsman, Y. Rosenwaks, G. Hodes, and D. Cahen, "Why lead methylammonium tri-iodide perovskite-based solar cells require a mesoporous electron transporting scaffold (but not necessarily a hole conductor)", *Nano Letters*, vol. 14, no. 2, pp. 1000–1004, 2014.

[79] G. A. Nemnes, C. Goehry, T. L. Mitran, A. Nicolaev, L. Ion, S. Antohe, N. Plugaru, and A. Manolescu, "Band alignment interfaces and charge transfer in rutile tio2 – ch3nh3pbi3-xclx", *Submitted to Phyisical Chemistry Chemical Physics (PCCP)*, 2015.

[80] H. J. Snaith, A. Abate, J. M. Ball, G. E. Eperon, T. Leijtens, N. K. Noel, S. D. Stranks, J. T.-W. Wang, K. Wojciechowski, and W. Zhang, "Anomalous hysteresis in perovskite solar cells", *The Journal of Physical Chemistry Letters*, vol. 5, no. 9, pp. 1511–1515, 2014.

[81] R. S. Sanchez, V. Gonzalez-Pedro, J.-W. Lee, N.-G. Park, Y. S. Kang, I. Mora-Sero, and J. Bisquert, "Slow dynamic processes in lead halide perovskite solar cells. characteristic times and hysteresis", *The Journal of Physical Chemistry Letters*, vol. 5, no. 13, pp. 2357–2363, 2014.

[82] W. Tress, N. Marinova, T. Moehl, S. M. Zakeeruddin, M. K. Nazeeruddin, and M. Gratzel, "Understanding the rate-dependent j-v hysteresis, slow time component, and aging in ch3nh3pbi3 perovskite solar cells: The role of a compensated electric field", *Energy Environ. Sci.*, vol. 8, pp. 995–1004, 3 2015.

[83] K. Ishigaki, M. Shiraishi, S. Suzuki, M. Asada, N. Nishiyama, and S. Arai, "Direct intensity modulation and wireless data transmission characteristics of terahertz-oscillating resonant tunnelling diodes", *Electronics letters*, vol. 48, no. 10, pp. 582–583, 2012.

School of Science and Engineering
Reykjavík University
Menntavegur 1
101 Reykjavík, Iceland
Tel. +354 599 6200
Fax +354 599 6201
www.ru.is